A Close Association of RyRs with Highly Dense Clusters of Ca^{2+}-activated Cl^- Channels Underlies the Activation of STICs by Ca^{2+} Sparks in Mouse Airway Smooth Muscle

Rongfeng Bao, Lawrence M. Lifshitz, Richard A. Tuft, Karl Bellvé, Kevin E. Fogarty, and Ronghua ZhuGe

Biomedical Imaging Group and Department of Physiology, University of Massachusetts Medical School, Worcester, MA 01655

Ca^{2+} sparks are highly localized, transient releases of Ca^{2+} from sarcoplasmic reticulum through ryanodine receptors (RyRs). In smooth muscle, Ca^{2+} sparks trigger spontaneous transient outward currents (STOCs) by opening nearby clusters of large-conductance Ca^{2+}-activated K^+ channels, and also gate Ca^{2+}-activated Cl^- ($Cl_{(Ca)}$) channels to induce spontaneous transient inward currents (STICs). While the molecular mechanisms underlying the activation of STOCs by Ca^{2+} sparks is well understood, little information is available on how Ca^{2+} sparks activate STICs. In the present study, we investigated the spatial organization of RyRs and $Cl_{(Ca)}$ channels in spark sites in airway myocytes from mouse. Ca^{2+} sparks and STICs were simultaneously recorded, respectively, with high-speed, widefield digital microscopy and whole-cell patch-clamp. An image-based approach was applied to measure the Ca^{2+} current underlying a Ca^{2+} spark ($I_{Ca(spark)}$), with an appropriate correction for endogenous fixed Ca^{2+} buffer, which was characterized by flash photolysis of NPEGTA. We found that $I_{Ca(spark)}$ rises to a peak in 9 ms and decays with a single exponential with a time constant of 12 ms, suggesting that Ca^{2+} sparks result from the nonsimultaneous opening and closure of multiple RyRs. The onset of the STIC lags the onset of the $I_{Ca(spark)}$ by less than 3 ms, and its rising phase matches the duration of the $I_{Ca(spark)}$. We further determined that $Cl_{(Ca)}$ channels on average are exposed to a $[Ca^{2+}]$ of 2.4 μM or greater during Ca^{2+} sparks. The area of the plasma membrane reaching this level is <600 nm in radius, as revealed by the spatiotemporal profile of $[Ca^{2+}]$ produced by a reaction-diffusion simulation with measured $I_{Ca(spark)}$. Finally we estimated that the number of $Cl_{(Ca)}$ channels localized in Ca^{2+} spark sites could account for all the $Cl_{(Ca)}$ channels in the entire cell. Taken together these results lead us to propose a model in which RyRs and $Cl_{(Ca)}$ channels in Ca^{2+} spark sites localize near to each other, and, moreover, $Cl_{(Ca)}$ channels concentrate in an area with a radius of ~600 nm, where their density reaches as high as 300 channels/μm^2. This model reveals that $Cl_{(Ca)}$ channels are tightly controlled by Ca^{2+} sparks via local Ca^{2+} signaling.

INTRODUCTION

In a variety of cells, the opening of one or a few ryanodine receptors (RyRs) in the membrane of endo/sarcoplasmic reticulum (ER/SR) produces highly localized, short-lived Ca^{2+} transients, designated as Ca^{2+} sparks or Ca^{2+} syntillas (Cheng et al., 1993; Nelson et al., 1995; Tsugorka et al., 1995; ZhuGe et al., 1998; DeCrescenzo et al., 2004; ZhuGe et al., 2006). These Ca^{2+} events comprise the elementary Ca^{2+} signals that underlie excitation–contraction coupling via either a calcium-induced calcium release mechanism in cardiac muscle or a mechanical coupling in skeletal muscle (Cannell et al., 1995; Lopez-Lopez et al., 1995; Klein et al., 1996). Ca^{2+} sparks in smooth muscle, however, may not serve as the "building block" of Ca^{2+} transient for excitation–contraction coupling (Nelson et al., 1995); rather they exert their influence by regulating the activity of Ca^{2+}-activated ion channels in the plasma membrane. We and others have demonstrated that Ca^{2+} sparks activate nearby large-conductance Ca^{2+}-activated K^+ channels (BK channels) to generate spontaneous transient outward currents (STOCs) in virtually all smooth muscle (Nelson et al., 1995; Bolton and Imaizumi, 1996; ZhuGe et al., 1998; Jaggar et al., 2000). The functional coupling between Ca^{2+} sparks and STOCs is critical for the regulation of smooth muscle contractility. When the BK channel β1 subunit, a subunit that increases the sensitivity of the pore-forming α subunit to Ca^{2+}, is genetically ablated or down-regulated, Ca^{2+} sparks less efficiently activate STOCs, resulting in the development of hypertension, urinary incontinence, and diabetic retinopathy in mice (Brenner et al., 2000; Petkov et al., 2001; Amberg and Santana, 2003; McGahon et al., 2007). A key cellular mechanism underlying such profound effects is the close proximity between RyRs and BK channels to form microdomains, where the activity of BK channels

Correspondence to Ronghua ZhuGe: ronghua.zhuge@umassmed.edu

The online version of this article contains supplemental material.

Abbreviations used in this paper: BK channel, large-conductance Ca^{2+}-activated K^+ channel; $Cl_{(Ca)}$ channel, Ca^{2+}-activated Cl^- channel; ER/SR, endo/sarcoplasmic reticulum; NPEGTA, *o*-nitrophenyl EGTA; RyR, ryanodine receptor; SM, signal mass; STIC, spontaneous transient inward current; STOC, spontaneous transient outward current.

The Rockefeller University Press $30.00
J. Gen. Physiol. Vol. 132 No. 1 145–160
www.jgp.org/cgi/doi/10.1085/jgp.200709933

is tightly controlled by Ca^{2+} sparks (Perez et al., 2001; ZhuGe et al., 2002).

In addition to causing STOCs, Ca^{2+} sparks turn on Ca^{2+}-activated Cl^- ($Cl_{(Ca)}$) channels to produce spontaneous transient inward currents (STICs) in many types of smooth muscle (ZhuGe et al., 1998; Gordienko et al., 1999; Williams and Sims, 2007). In these cells, activation of STICs lead to membrane depolarization (Williams and Sims, 2007), an opposite response to the activation of STOCs. Therefore it is physiologically important to understand the cellular mechanism determining the coupling between Ca^{2+} sparks and STICs. However, little information is available as to how Ca^{2+} sparks activate STICs. A key question to be resolved is the spatial relationship between RyRs and $Cl_{(Ca)}$ channels that controls their functional coupling. There are several reasons that the relationship between RyRs and $Cl_{(Ca)}$ channels might be different from that between RyRs and BK channels. For instance, $Cl_{(Ca)}$ channels are thought to be much more sensitive to Ca^{2+} than BK channels (Singer and Walsh, 1987; Pacaud et al., 1992; Tanaka et al., 1997; Piper and Large, 2003) so they could localize far away from RyRs and still be activated by Ca^{2+} sparks. Also, in rat portal vein, Ca^{2+} sparks activated BK channels to produce STOCs but they failed to activate $Cl_{(Ca)}$ channels and STICs (Mironneau et al., 1996). Finally, at resting membrane potential Ca^{2+} sparks simultaneously activate BK channels and $Cl_{(Ca)}$ channels, resulting in biphasic currents with an STOC component always preceding an STIC component (ZhuGe et al., 1998). In light of these differences, it is essential to examine experimentally the spatial relationship between RyRs and $Cl_{(Ca)}$ channels. An attractive approach to exploring this relationship would be to visualize both RyRs and $Cl_{(Ca)}$ channels in the cells with immunolight and immunoelectron microscopy. Unfortunately, the gene(s) encoding $Cl_{(Ca)}$ channels are yet to be discovered, so it is currently impossible to localize these channels in these cells.

Here, we have used a variety of analyses of electrophysiological and imaging data to investigate the organization of RyRs and $Cl_{(Ca)}$ channels underlying the functional coupling of Ca^{2+} sparks and STICs in mouse airway smooth muscle cells. First, Ca^{2+} sparks were recorded in isolated single cells with a wide-field imaging microscope at high speed and, at the same time, STICs were monitored using whole-cell patch clamp. A signal mass approach (ZhuGe et al., 2000) was employed to quantify the total amount of Ca^{2+} release from Ca^{2+} sparks (via RyRs) and the underlying Ca^{2+} currents ($I_{Ca(spark)}$), allowing us to analyze quantitatively the relationship between Ca^{2+} sparks and STICs. Second, we characterized $Cl_{(Ca)}$ channels using flash photolysis of caged Ca^{2+}. To our surprise, $Cl_{(Ca)}$ channels are highly insensitive to Ca^{2+} in these cells compared with the reports in other types of smooth muscle. Third, we devised an approach to estimating the conductance underlying STICs ($g_{(STIC)}$) and its relationship with voltage; with this relationship we estimated the $[Ca^{2+}]$ "seen" by $Cl_{(Ca)}$ channels underlying STICs. Fourth, we performed reaction-diffusion simulations to derive the spatio-temporal profile of $[Ca^{2+}]$ from Ca^{2+} sparks with measured $I_{Ca(spark)}$. Combining this profile with the estimate of $[Ca^{2+}]$ sensed by $Cl_{(Ca)}$ channels, we determined the area occupied by these channels near the spark sites to generate an STIC. Finally, we estimated that the $Cl_{(Ca)}$ channels residing in sparks sites could account for all the channels present in the entire cell; that is, $Cl_{(Ca)}$ channels could be exclusively near spark sites.

With these studies, we found that in Ca^{2+} spark sites, RyRs and $Cl_{(Ca)}$ channels localize near to each other, and $Cl_{(Ca)}$ channels concentrate in an area with a radius of ~600 nm, where their density reaches as high as 300 channels/μm^2. These findings reveal that $Cl_{(Ca)}$ channels are tightly controlled by Ca^{2+} from nearby RyRs, uncovering a new property of Ca^{2+} microdomains in smooth muscle.

MATERIALS AND METHODS

Preparation of Airway Smooth Muscle Cells from Mouse

Male Swiss Webster mice, of age 6–9 wk, were killed with intraperitoneal injection of a lethal dose of sodium pentobarbital (50 mg kg^{-1}), in accordance with the guidelines of the Animal Care Committee of the University of Massachusetts Medical School. After each animal was unresponsive to any applied stimulus, trachea was quickly removed and placed in prechilled dissociation solution, consisting of (in mM) 136 NaCl, 5.36 KCl, 0.44 KH_2PO_4, 4.16 $NaHCO_3$, 0.34 Na_2HPO_4, 5 mM $MgCl_2$, 20 mM HEPES, and 10 glucose (pH 7.1). The trachea was dissected free from the surface of connective tissues and incubated in the dissociation medium without $MgCl_2$ but plus papain 30 U/ml (Sigma-Aldrich), 0.2 mM DTT, and 0.02 mM EDTA at room temperature for 30 min. The tissue was then incubated at 32°C for another 6 min with fresh zero $MgCl_2$ dissociation medium containing 3 U/ml collagenase 1A (Sigma-Aldrich), 0.2 mg/ml proteinase E (Sigma-Aldrich), 0.1 mg/ml DNAase 1 (Willington), and 1 mg/ml amino acid-free BSA (Sigma-Aldrich). Finally, the tissue was agitated with a fire polished wide-bore glass pipette to release the cells. The isolated single airway smooth muscle cells were spindle-shaped with a length of around 150 μm, and used the same day at 25°C.

Patch-clamp Recording

Membrane currents were recorded using the tight-seal, conventional whole-cell configuration. The extracellular solution contained (in mM) 130 NaCl, 5.5 KCl, 2.2 $CaCl_2$, 1 $MgCl_2$, 10 HEPES, pH adjusted to 7.4 with NaOH. The pipette solution contained (in mM) 139 KCl, 1 $MgCl_2$, 3 Na_2ATP, 10 HEPES, and 0.05 fluo-3 K_5 (Invitrogen), pH to 7.3 with KOH. For experiments in Fig. 5, the bath solution contained (in mM) 130 NaCl, 5.5 TEA-Cl, 2.2 $CaCl_2$, 1 $MgCl_2$, 10 HEPES, pH adjusted to 7.4 with NaOH; and the pipette solution contained (in mM) 75 CsCl, 64 Cs-glutamate, 1 $MgCl_2$, 10 HEPES, 3 Na_2ATP, and 0.05 fluo-3 K_5 (pH adjusted to 7.3 with CsOH). Whole-cell currents were recorded at desired holding potentials and low-pass filtered using the Axopatch 1D amplifier (200 Hz cutoff) and then digitally sampled at 1 kHz and stored for analysis. Events were counted as STICs if their amplitude exceeded twofold of RMS of the baseline, and their area

under curve was >10 fold of the value of RMS as detected by Mini Analysis Program (Snaptosoft). The events were then checked by visual inspection to eliminate anomalies such as multiple events overlapping in time or excessively noisy traces.

Imaging and Measurement of Ca^{2+} Sparks

Fluorescent images were obtained using fluo-3 (Invitrogen) as the calcium indicator and a custom-built wide-field, high-speed digital imaging system, which is described in detail elsewhere (ZhuGe et al., 1999). Rapid imaging was made possible by using a cooled high-sensitivity, charge-coupled device camera (128 × 128 pixels) developed in conjunction with MIT Lincoln Laboratory. The camera was interfaced to a custom-made, inverted microscope equipped with a 40× oil immersion lens (NA 1.3); each pixel covered a 333 nm × 333 nm area of the cell. The 488-nm line of a multiline argon laser provided fluorescence excitation for the indicator fluo-3, and a laser shutter controlled the exposure duration. Emission of the Ca^{2+} indicator was monitored at wavelengths >500 nm. To obtain a constant concentration of Ca^{2+} indicator, fluo-3 (50 μM) was delivered through the patch pipette, and measurements were not commenced until 10–15 min after disruption of the patch. After this time no significant change in background fluorescence was detected. Subsequent image processing and analysis were performed off-line using a custom-designed software package, running on a Linux workstation.

Two measures of Ca^{2+} sparks were employed: the conventional fluorescence ratio, $\Delta F/F_0$, within a restricted area; and the change in total fluorescence, $F - F_o$, over a larger volume, also designated as the Ca^{2+} signal mass, which is proportional to the total quantity of Ca^{2+} released into the cytosol. As demonstrated previously (ZhuGe et al., 2000), $\Delta F/F_0$ is a poor indicator of local $[Ca^{2+}]_{cyto}$ generated by Ca^{2+} sparks. In the present study, this measure was used mainly for identifying events. Both conventional fluorescence ratio and Ca^{2+} signal mass measurements have been previously described in detail (ZhuGe et al., 2000); a brief description follows. For the fluorescence ratio measure, the fluo-3 images, with pixel size 333 × 333 nm, were first smoothed by convolution with a 3 × 3 pixel approximation to a two-dimensional Gaussian (σ = 1 pixel). Fluorescence ratios were then calculated and expressed as a percentage on a pixel to pixel basis from the equation:

$$\Delta F/F_0(\%) = 100 \times (F - F_0)/F_0 = 100 \times \frac{(F(x,y,t) - F_0(x,y))}{F_0(x,y)}, \quad (1)$$

where F is the fluorescence at each pixel in the time series and F_0 is the "resting" level derived from the fluorescence time series by computing the median pixel value during quiescent times at each F(x,y). During a spark, the single pixel that had the highest fluorescence ratio is designated as the epicenter pixel (Fig. 8). The second measure, the Ca^{2+} signal mass, for each spark was computed from the two-dimensional, wide-field fluorescence images of fluo-3 according to the equations:

$$\text{Total Fluorescence, } F^T(t) = \sum_{\Delta x=-20}^{+20} \sum_{\Delta y=-20}^{+20} \left[F(x + \Delta x, y + \Delta y, t\right] \quad (2)$$

$$\text{Signal mass, } sm(t) = G(F^T(t) - F^T(t_0)). \quad (3)$$

The signal mass (sm(t)) is the product of the detector gain (G) times the change in total fluorescence (F^T) summed over a square region of 40 × 40 pixels, surrounding the spark epicenter pixel (x,y) as determined from the $\Delta F/F_0$ images from Eq. 1. The number of moles of Ca^{2+} bound to fluo-3 was calculated by the equation: $2.44 \cdot sm(t)/(6.022 \cdot 10^{23})$ moles, where 2.44 is a calibration factor previously determined (ZhuGe et al., 2000). Since there may be other Ca^{2+} buffers in the patched and dialyzed cells, Ca^{2+}-bound fluo-3 provides a minimum value for the total Ca^{2+} released. To correct for the contribution of endogenous Ca^{2+} buffers to the signal mass, we characterized these buffers using flash photolysis of caged Ca^{2+} as detailed in the following section.

Flash Photolysis of Caged Ca^{2+} and Estimate of Fixed Ca^{2+} Buffers

A 100-ms exposure of UV light (λ = 351 nm) from an argon ion ultraviolet laser was coupled to the epi-illumination port of our high-speed inverted microscope, and focused on the cell through a Nikon 40× UV, 1.3 NA, oil immersion lens. The UV beam was passed through an optical path such that it was restricted to illuminate a circle 160 μm in diameter on the cell. The cell under study was located in the center of this illumination area so that the entire cell was illuminated, resulting in an elevation in $[Ca^{2+}]$ that sustained for several seconds after uncaging.

NPEGTA (*o*-nitrophenyl EGTA) was dialyzed into cells via the patch pipette so that its concentration and resultant $[Ca^{2+}]$ upon photolysis could be determined. In the patch pipette, 50 μM ryanodine was also included to minimize the involvement of calcium-induced calcium release upon an increase in $[Ca^{2+}]$ after photolysis. In our preliminary study, we varied the laser settings to determine the photon density that was sufficient to uncage all the NPEGTA present in the cells. We found that a (cell) specimen illumination of ~400 w/cm^2 for 100 ms was sufficient for this purpose, since a second exposure within 1 s of the first, at the same power and duration, failed to increase $[Ca^{2+}]_{cyto}$ and $I_{Cl(ca)}$. This level of photon density does not produce measurable phototoxicity since when cytosolic NPEGTA was absent or <10 μM, photolysis did not trigger $I_{Cl(ca)}$ (see Fig. 4). Thus we employed this laser setting for all the flash photolysis experiments in the present study.

To estimate endogenous fixed Ca^{2+} buffers (mobile buffers are expected to be dialyzed out the cells under whole-cell configuration and thus are not considered in the present study), we first measured $[Ca^{2+}]_{cyto}$ with fluo-3 upon flash photolysis of caged NPEGTA by an equation similar to that derived by Maravall et al. (2000):

$$[Ca^{2+}]_{cyto} = Kd_{Fluo3} \times \frac{\frac{R}{R_{max}}}{1 - \frac{R}{R_{max}}}, \quad (4)$$

where Kd_{Fluo3} is taken as 1.1 μM (Harkins et al., 1993), R equals to the fluorescence ratio before and after photolysis of various [NPEGTA], and R_{max} is the ratio when [NPEGTA] is 833 μM. In the example shown in Fig. 1 A, R_{max} was 12 and on average this value was 11.58 ± 1.55 (n = 5). These values are close to the theoretical value of R_{max} for a resting $[Ca^{2+}]_{cyto}$ of 104 ± 9 nM (n = 6 cells) as measured with fura-2 using a microfluorimeter (ZhuGe et al., 1999), suggesting that photolysis of NPEGTA at this level produces a saturated $[Ca^{2+}]$ for fluo-3.

Next, we compared the relationship between measured $[Ca^{2+}]_{cyto}$ and total Ca^{2+} released upon flash photolysis of various [NPEGTA], i.e., $[Ca^{2+}]_{\Delta T}$ (Fig. 1 B). To do so, we first examined whether NPEGTA affects resting $[Ca^{2+}]_{cyto}$ and then determined the fraction of Ca^{2+}-bound NPEGTA. For the cells shown in Fig. 1 A, when [NPEGTA] was preset in the range of 0–200 μM, averaged fluorescence per pixel was constant, fitted linearly with a slope of −0.018, which was not different from 0 (P = 0.728). At 833 μM, the averaged fluorescence per pixel decreased to 70% of the control value. Using the microfluorimeter with fura-2, we estimated that $[Ca^{2+}]_{cyto}$ was 108 ± 11 (n = 6) and 84 ± 9 nM (n = 5) in the presence of 200 μM and 833 μM NPEGTA, respectively. (One possible caveat for examining the effect of NPEGTA on $[Ca^{2+}]_{cyto}$ is that NPEGTA in the cytosol could be slowly photolyzed by the UV light from Arc lamp in the microfluorimeter. However, this

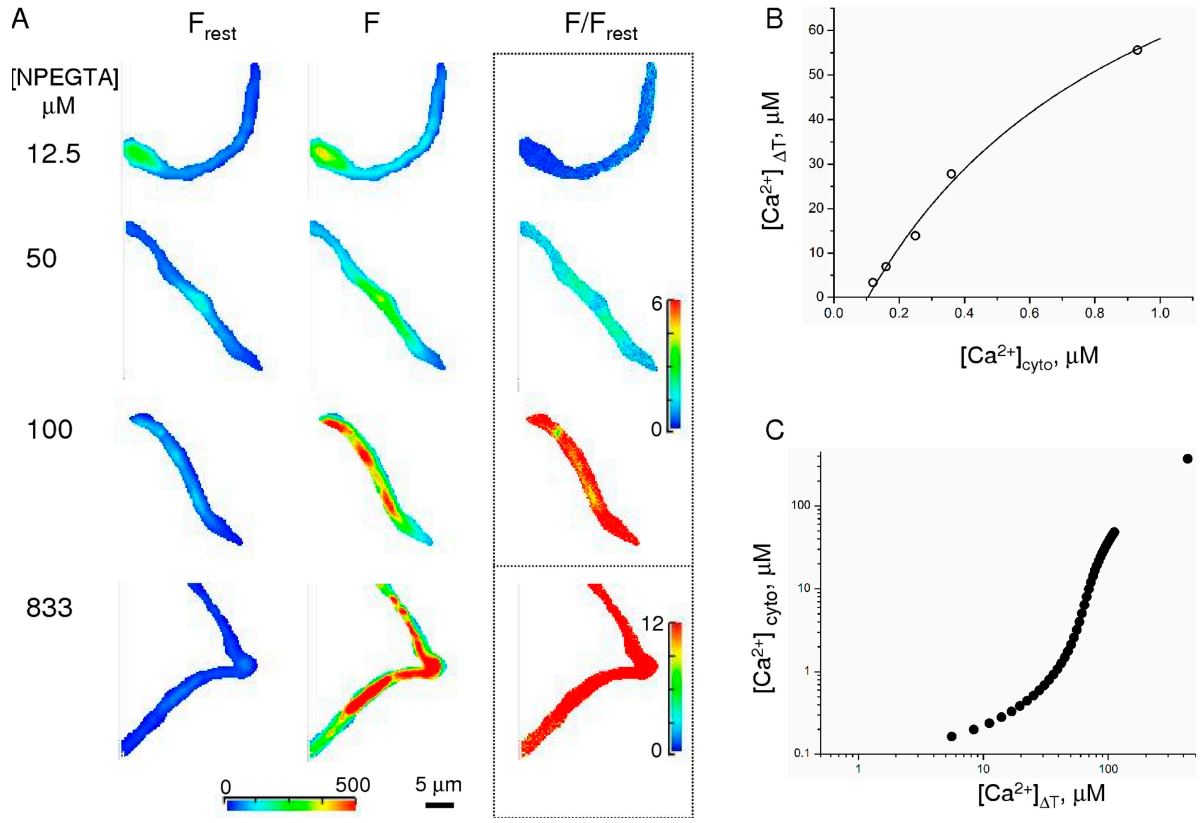

Figure 1. Estimate of endogenous fixed Ca^{2+} buffer with flash photolysis of NPEGTA. (A) $[Ca^{2+}]_{cyto}$ is increased throughout the cell upon flash photolysis of caged Ca^{2+} compound NPEGTA. The voltage-clamped cells were loaded, via patch pipettes, with variable [NPEGTA] and 50 μM fluo3, and liberation of Ca^{2+} from NPEGTA was accomplished by flash photolysis of 100 ms (see Materials and methods for detail). Examples of fluorescence change upon photolysis of NPEGTA at the concentrations shown on the left. The images were acquired at a rate of 20 Hz with an exposure time of 5 ms pre- and post-flash photolysis. Images shown are fluorescence before laser illumination (F_{rest}), the first frame after the illumination (F), and their ratios, i.e., $F/F_{rest} = R$, with 20% correction for bleaching. The color scale under fluorescence images denotes absolute readout in the CCD camera, and the two on the right of ratio images are for [NPEGTA] at 833 μM and at all other concentrations, respectively. (B). Relationship between $[Ca^{2+}]_{cyto}$ estimated with fluo-3 and the total calcium released upon photolysis of NPEGTA, i.e., $[Ca^{2+}]\Delta_T$. $[Ca^{2+}]_{cyto}$ was calculated using results from experiments in A with Eq. 4 in the text, and $[Ca^{2+}]\Delta_T$ was determined as 52–57% of [NPEGTA] in the patch pipette given our experimental conditions (see Materials and methods). To simplify the fitting with Eq. 5, $[Ca^{2+}]_{cyto}$ is plotted along the x axis and $[Ca^{2+}]\Delta_T$ along the y axis. (C). The relationship between $[Ca^{2+}]_{cyto}$ and $[Ca^{2+}]\Delta_T$ in the absence of fluo-3. Data were derived based on the estimate of endogenous fixed Ca^{2+} buffer determined in B.

possibility was ruled out in our conditions by the observations that (a) $[Ca^{2+}]_{cyto}$ in the presence of NPEGTA was as stable as when NPEGTA was absent, and (b) $[Ca^{2+}]_{cyto}$ was the same when measured 1 min apart in the presence of NPEGTA.) Therefore, two lines of data indicate that up to 200 μM, NPEGTA does not affect resting $[Ca^{2+}]_{cyto}$, and at 833 μM it modestly decreases the $[Ca^{2+}]_{cyto}$. Given that (a) NPEGTA has a K_d of 80 nM in its caged form, and (b) all of the loaded NPEGTA is photolyzed, $[Ca^{2+}]_{\Delta T}$ is expected to be ~57% of [NPEGTA] loaded in the patch pipette when the concentration is <200 μM, and 52% when it is at 833 μM.

Assuming a simple one-compartment model of cellular $[Ca^{2+}]$ dynamics, $[Ca^{2+}]_{\Delta T}$ can be described according to an equation:

$$[Ca^{2+}]_{\Delta T} = [Ca^{2+}]_{cyto} + \frac{[Fluo3]_T \times [Ca^{2+}]_{cyto}}{Kd_{Fluo3} + [Ca^{2+}]_{cyto}} + \frac{[B]_T \times [Ca^{2+}]_{cyto}}{Kd_B + [Ca^{2+}]_{cyto}} - [Ca^{2+}]_{T0}, \quad (5)$$

where $[Fluo3]_T$ = 50 μM, Kd_{Fluo3} is 1.1 μM, $[Ca^{2+}]_{T0}$ the total cytosolic $[Ca^{2+}]$ before photolysis, $[B]_T$ the concentration of endogenous fixed buffer, and Kd_B the equilibrium dissociation constant for this buffer. Fitting the data (open circles in Fig. 1 B) with Eq. 5 using a Levenberg-Marguardt nonlinear least-squares optimization method yielded $[B]_T$ = 81 μM, Kd_B = 0.66 μM, and $[Ca^{2+}]_{T0}$ = 15.6 μM (χ^2 = 11.715; r = 0.9967). With these values, we estimate the binding ratio (κ) of this buffer to be 92, using

$$\kappa = \frac{[B]_T \times Kd_B}{([Ca^{2+}] + Kd_B)^2}$$

(Zhou and Neher, 1993), with $[Ca^{2+}]$ as 104 nM. For the same calculation, κ for 50 μM fluo-3 is 38. Therefore, the values of signal mass and resulting $I_{Ca(spark)}$ as estimated by fluo-3 fluorescence were adjusted with a correction factor of 3.45, i.e., (1 + 92 + 38)/38, to reflect $I_{Ca(spark)}$ and the total amount of Ca^{2+} released during Ca^{2+} sparks under physiological conditions in these cells.

Given these parameters on the endogenous fixed Ca^{2+} buffer, we can further estimate $[Ca^{2+}]_{cyto}$ upon photolysis of NPEGTA in the absence of fluo-3 (Fig. 1 C). These estimates were used to set $[Ca^{2+}]_{cyto}$ when Ca^{2+} sensitivity of $Cl_{(Ca)}$ channels was probed (Fig. 4).

Simulation of the Spatial-Temporal Profile of [Ca^{2+}] Arising from Ca^{2+} Sparks

To gain insight into the role of Ca^{2+} sparks triggering STICs, we modeled a simplified cell, simulated Ca^{2+} sparks, and examined the spatial and temporal profile of free [Ca^{2+}] that resulted at the plasma membrane where $Cl_{(Ca)}$ channels are located. Finite difference approximations were used to solve a set of partial differential equations for the reaction-diffusion kinetics in a cylindrically symmetric coordinate system. The details of this approach were described elsewhere (ZhuGe et al., 2002), and it has been used before to analyze the spatial-temporal profile of [Ca^{2+}] resulting from Ca^{2+} sparks in amphibian gastric smooth muscle, chromaffin cells, and nerve terminals (ZhuGe et al., 2002; DeCrescenzo et al., 2004; ZhuGe et al., 2006). The cell was modeled as a cylinder, 5 μm in diameter and 5 μm in length. The Ca^{2+} release site was modeled as a small cylinder, 20 nm in diameter and height, with the cylinder end located 20 nm from the plasma membrane (Somlyo and Franzini-Armstrong, 1985). The simulation included the following: fluo-3 as the sole mobile buffer (50 μM, K_d = 1.1 μM, $k_{on} = 8 \times 10^4$ $mM^{-1}s^{-1}$, k_{off} = 90 s^{-1}, D = 25 $\mu m^2 s^{-1}$); Nondiffusible fixed buffer at 81 μM (K_d = 0.66 μM, $k_{on} = 8 \times 10^4$ $mM^{-1}s^{-1}$, k_{off} = 52.8 s^{-1}). Endogenous mobile buffers are expected to be washed out via the patch pipette and thus not included in the simulations.

Statistics

Results are presented as mean ± SEM, unless otherwise indicated. N denotes the number of cells and n the number of events, i.e., Ca^{2+} spark or STIC. Student's *t* tests and ANOVA, when appropriate, were used to compare the means from different conditions.

Online Supplemental Material

The online supplemental material is available at www.jgp.org/cgi/content/full/jgp.200709933/DC1. Fig. S1 shows reaction-diffusion simulations, demonstrating that the endogenous fixed Ca^{2+} buffer measured with the flash photolysis of NPEGTA exerts a minimal effect on both the rise and decay phase of estimated $I_{Ca(spark)}$. Fig. S2 examines the correlation between STICs and Ca^{2+} sparks using $\Delta F/F_0$ in the epicenter pixel, i.e., the conventional fluorescence ratio.

RESULTS

$I_{Ca(spark)}$ Has a Linear Rise and an Exponential Decay

Knowledge of the spatio-temporal profile of [Ca^{2+}] generated by the opening of RyRs during a Ca^{2+} spark is critical to an understanding of the spatial relationship between RyRs underlying Ca^{2+} sparks and $Cl_{(Ca)}$ channels for STICs. But it has not been possible previously to directly measure this profile for at least two reasons. First, Ca^{2+} and Ca^{2+} indicator (fluo-3) do not necessarily come into equilibrium in a microdomain where there could exist a huge Ca^{2+} gradient (Stern, 1992; Naraghi and Neher, 1997). And second, the fluorescence signal from an area of even a single pixel is an average of an underlying gradient of [Ca^{2+}] in the microdomain that could be below the spatial resolution of light microscope (ZhuGe et al., 2000). To circumvent these difficulties, in the present study we employed a strategy that we had developed to estimate the [Ca^{2+}] profile produced by Ca^{2+} sparks in amphibian smooth muscle and by Ca^{2+} syntillas in nerve terminals and chromaffin cells

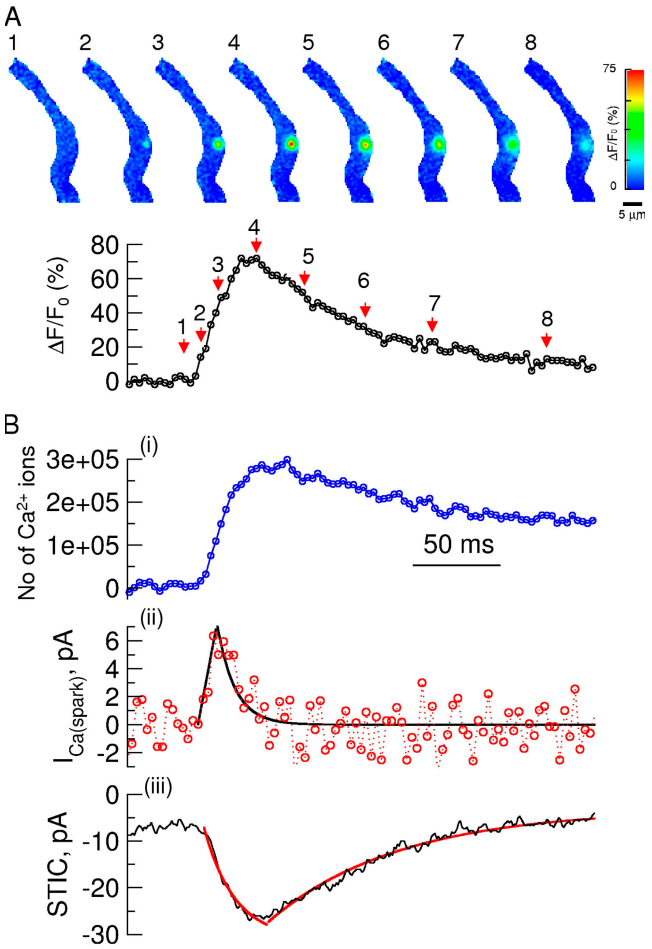

Figure 2. An STIC evoked by a Ca^{2+} spark recorded with high-speed wide-field imaging. (A) Images display the spatio-temporal evolution of a single Ca^{2+} spark and the trace exhibits the time course of change in fluorescence at the epicenter pixel of the spark. The cell was voltage-clamped at a membrane potential of −80 mV, i.e., E_K, and the images were acquired at a rate of 333 Hz with an exposure time of 3 ms. Cytosolic Ca^{2+} was measured using fluo-3 (50 μM), which was introduced into the cell in the K^+ form through the patch pipette. Changes in Ca^{2+} concentration in the images are expressed as $\Delta F/F_0$ (%) and displayed on a pseudocolor scale calibrated at the right of images. Numbers above the images correspond to the numbers in the bottom panel and indicate the time at which the images were obtained. (B) The time course of signal mass (i), its time derivative calibrated to give the underlying Ca^{2+} current flowing from the intracellular Ca^{2+} store into the cytosol, i.e., $I_{Ca(spark)}$ (ii) for the spark shown in A, and the corresponding STIC (iii). The abscissa in B and in the bottom panel of A has the same scale. Black lines in the panel ii are fits of linear function to the rise, and of single exponential function to the decay with a time constant of 13 ms. Red lines in the bottom panel represent fits of STIC rise with $I(t) = I_{max}(1 - \exp(-t/\text{tau}))$ with a time constant of 26 ms, and of its decay by single exponential function with a time constant of 91 ms. Note that the endogenous fixed Ca^{2+} buffer as estimated in Fig. 1 was taken into account in this and following figures' calculation of signal mass and $I_{Ca(spark)}$.

(ZhuGe et al., 2002, 2006; DeCrescenzo et al., 2004). This strategy begins by estimating $I_{Ca(spark)}$, i.e., Ca^{2+} current through RyRs during a Ca^{2+} spark. This is made

TABLE I

Properties of Ca^{2+} Sparks and STICs

	SM (Ca^{2+} ions)[b]	$I_{Ca(spark)}$	$\Delta F/F_0$ (%)[c]
(A) Ca^{2+} sparks[a]			
Amplitude	276,000 ± 46,000 (29)[e]	8.5 ± 1.2[f] (29)	46 ± 5 (23)
	235,000 ± 34,500 (159)	4.1 ± 0.5[g] (159)	
Duration (ms)[d]		44 ± 5 (23)	162 ± 13 (23)
Rise Time (ms)		9 ± 2 (29)	24 ± 2 (23)
Tau_{decay} (ms)		12 ± 2 (23)	55 ± 5 (23)
	Amplitude (pA)	Tau_{rise} (ms)	Tau_{decay} (ms)
(B) STICs[a]	35 ± 5 (138)	21 ± 3 (97)	98 ± 8 (77)

[a]Recorded simultaneously at −80 mV.
[b]Corrected for endogenous fixed Ca^{2+} buffer.
[c]Fluorescence change in the epicenter pixel of the sparks.
[d]Time between the onset of the event to 92% of the decay (i.e., 2.5 times of decay Tau).
[e]Number in parentheses depicts the number of events.
[f]Measured by time differentiation of SM; unit, pA.
[g]Estimated by fitting 10–90% of SM rise phase; unit, pA.

possible with the signal mass approach that can directly measure the total quantity of Ca^{2+} released during a Ca^{2+} spark with high-speed wide-field imaging. At its simplest, signal mass can be viewed as a product of the amplitude and duration of $I_{Ca(spark)}$ with a proportionality factor. Thus, time differentiation of the signal mass gives rise to the time course of $I_{Ca(spark)}$. This time course can then be used as a Ca^{2+} source in a reaction-diffusion simulation to deduce the spatio-temporal profile of $[Ca^{2+}]$ induced by Ca^{2+} sparks.

To reveal the amplitude and waveform of $I_{Ca(spark)}$, we imaged Ca^{2+} sparks at a speed of 333 Hz with exposure of 3 ms. Fig. 2 displays an example of Ca^{2+} sparks recorded at this speed. The images in A exhibit the spatial and temporal evolution of the Ca^{2+} spark, and the time course of change in fluorescence ratio from the epicenter pixel is shown in the bottom panel. The total quantity of Ca^{2+} released from this spark and the underlying $I_{Ca(spark)}$ are shown in the top and middle panels of Fig. 2 B, respectively. For this spark, the value of signal mass was 286,000 Ca^{2+} ions after compensating for the estimated endogenous fixed Ca^{2+} buffer (see Materials and methods). Interestingly, the rising phase of signal mass consisted of two components, a fast one followed by a slow one. These two components corresponded to the two phases in $I_{Ca(spark)}$, i.e., a rising phase that can be roughly fitted with a linear function with 9 ms from the onset to the peak, and a decay phase that can be fitted with an exponential function with a tau of 13 ms. The duration of $I_{Ca(spark)}$, i.e., from the onset of an event to the point when the current decays ∼92% (equal to 2.5 times of the decay constant), was ∼39 ms and the peak amplitude of this current was ∼6.4 pA.

On average (Table I), it was found that (a) a Ca^{2+} spark releases 276,000 ± 46,000 Ca^{2+} ions, (b) $I_{Ca(spark)}$ has a peak amplitude of 8.5 ± 1.2 pA, and (c) this current reaches peak within 9 ± 2 ms and decays with a single exponential function with a tau of 12 ms ± 2 ms. These values were calculated including the effect of the estimated endogenous fixed Ca^{2+} buffer in this type of cell. We should point out that these sparks were for high signal to noise characteristics, and may not reflect the complete distribution of events (see below). Also, since the kinetics of binding of the endogenous fixed Ca^{2+} buffer are not yet determined, their effect on the observed rise and decay of $I_{Ca(spark)}$ cannot be directly incorporated. However, even if we assume that the buffer has the same diffusion-limited on-rate as fluo-3 (i.e., it is a fast buffer), it has minimal influence on either the rise or the decay phase of the estimate of $I_{Ca(spark)}$ (see Fig. S1, available at http://www.jgp.org/cgi/content/full/jgp.200709933/DC1). Therefore, the measured waveform of $I_{Ca(spark)}$ most likely reflects the underlying Ca^{2+} current from the opening of RyRs during Ca^{2+} sparks under physiological conditions in these cells.

Ca^{2+} Sparks Activate STICs

Fig. 2 also demonstrates a close temporal relationship between Ca^{2+} sparks and STICs. The onset of this Ca^{2+} spark coincided with the STIC. On average there is a delay between spark and STIC of ∼3 ms, which is consistent with the notion that Ca^{2+} sparks are the causal signals of STICs (ZhuGe et al., 1998). This notion is reinforced by the following observations. (a) Ryanodine (100 μM), an inhibitor of ryanodine receptor, blocked both Ca^{2+} sparks and STICs (unpublished data); and (b) niflumic acid (100 μM), a $Cl_{(Ca)}$ channel blocker, abolished STICs but did not affect the frequency and amplitude of Ca^{2+} sparks (unpublished data). The blockage of STICs by niflumic acid also indicates that these currents are carried by Cl^- flux passing through $Cl_{(Ca)}$ channels. (The reversal of STIC polarity around E_{Cl} is another indication of this conclusion, see Fig. 5 A.) Taken together, these results demonstrate that Ca^{2+}

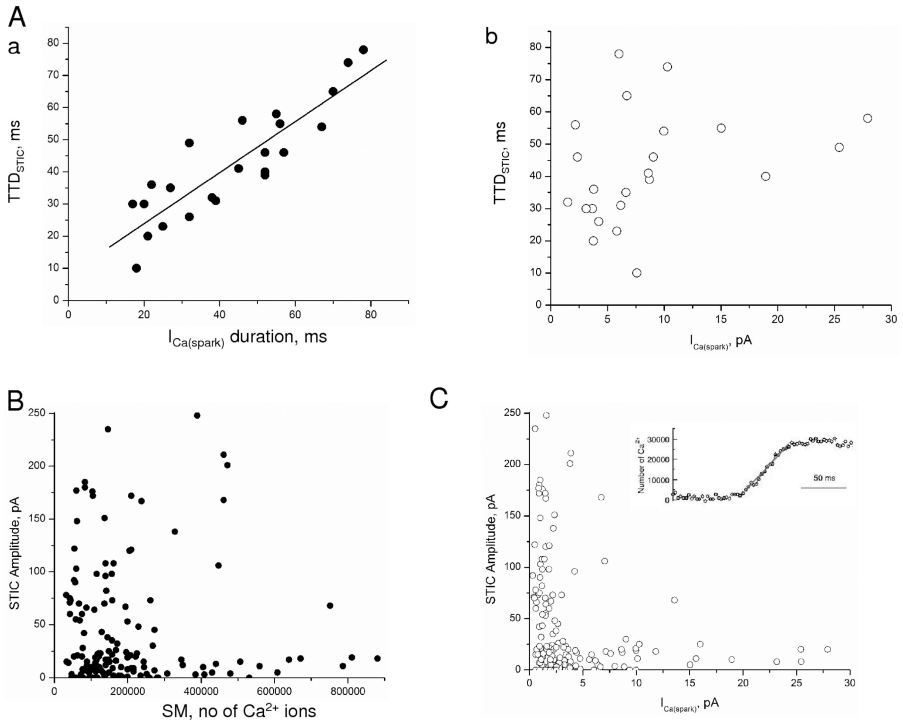

Figure 3. Quantitative relationships between Ca^{2+} sparks and STICs. (A, a) Time between the onset of the STIC and the onset of its decay, designated as time to onset of decay (TTD_{STIC}), is close to the duration of $I_{Ca(spark)}$. The graph displays the scatter plot and linear fit of these variables (n = 23, r = 0.879, P < 0.0001). The duration of $I_{Ca(spark)}$ was measured as the sum of the rise time, obtained by linear fitting of the rising phase, and 2.5 times of the decay constant. (A, b) TTD_{STIC} is independent of the peak amplitude of $I_{Ca(spark)}$ (n = 23, r = 0.316, P > 0.14). (B) No correlation between Ca^{2+} spark signal mass (SM) and STIC amplitude (r = 0.056 and P = 0.487 [n = 159] for all sparks; r = −0.053 and P = 0.551 [n = 133] for STIC-generating sparks only). To increase the number of data in this panel and panel C, a subset of Ca^{2+} sparks were recorded at a speed of 100 Hz, an acquisition rate sufficient to accurately estimate the signal mass since this signal sustains at its plateau for additional ∼30 ms after reaching the peak (see Fig. 2). Signal mass is expressed in term of the number of Ca^{2+} liberated during Ca^{2+} sparks. Note that the values of signal mass from a subset of Ca^{2+} sparks intersect with the abscissa, being designated as STIC-less sparks in the text. (C) Lack of correlation between $I_{Ca(spark)}$ and STIC amplitude (r = −0.112 and P = 0.093 [n = 159] for all sparks; r = −0.248 and P = 0.004 [n = 133] for STIC-generating sparks only). This analysis pools data from two sets of Ca^{2+} sparks. For one set, $I_{Ca(spark)}$s were estimated by the first time differentiation of signal mass as shown in Fig. 2. For another one where $I_{Ca(spark)}$s could not be resolved by the differentiation because of low signal-noise ratio of signal mass, they were obtained by linear fitting 10–90% of the rising phase of signal mass (Inset). Though the latter approach tends to underestimate the peak amplitude of underlying $I_{Ca(spark)}$, their correlation with STIC amplitude is not different from that when $I_{Ca(spark)}$ was estimated with the first approach.

sparks, resulting from the opening of RyRs, activate $Cl_{(Ca)}$ channels to generate STICs in airway smooth muscle from mouse.

$Cl_{(Ca)}$ Channels Localize in Proximity to RyRs and Do Not Distribute Homogeneously on the Surface Membrane

High speed imaging of Ca^{2+} sparks and analysis of the resulting signal mass allows us to quantitatively examine the relationship between Ca^{2+} sparks and their corresponding STICs, which, in turn, could give insight into the molecular organization of underlying RyRs and $Cl_{(Ca)}$ channels in the spark sites. As shown in the example of Fig. 2, $I_{Ca(spark)}$ increased over time, as did the corresponding STIC. But $I_{Ca(spark)}$ reached its peak before the STIC. As $I_{Ca(spark)}$ declined, the STIC kept rising until $I_{Ca(spark)}$ returned to the baseline; at that point the STIC entered its decay phase. From this relationship, it is clear that the rise time of an STIC, i.e., from the onset of the current to the onset of the current decay, correlates with the duration of $I_{Ca(spark)}$, which reflects the open time of RyRs underlying Ca^{2+} sparks. On average, the duration of $I_{Ca(spark)}$ was 44 ± 5 ms, which is the same as the rise time of corresponding STICs (42 ± 4 ms) (Fig. 3 A, a; r = 0.879, P < 0.0001, n = 23). (In comparison, the rise time of $\Delta F/F_0$ [24 ± 2 ms] is faster than that of the corresponding STICs [Table I; Fig. S2].) On the other hand, the amplitude of $I_{Ca(spark)}$ bears no correlation with the rise time of the STICs (Fig. 3 Ab; r = 0.316, P > 0.14), and neither does Ca^{2+} spark amplitude as estimated by $\Delta F/F_0$ (Table I; Fig. S2). The close match in the rise time of the STIC and the duration of the $I_{Ca(spark)}$ suggests that $Cl_{(Ca)}$ channels for STICs may localize closely to RyRs so that activation of $Cl_{(Ca)}$ channels is maintained as long as the RyRs are open; alternatively, this relationship implies that $Cl_{(Ca)}$ channels could occupy a sizable area, spreading around RyRs so the longer the RyRs stay open, the more of them are recruited and activated by diffusing of Ca^{2+}.

To distinguish between these two possibilities, we further analyze the relationship between Ca^{2+} sparks and their corresponding STICs by examining the correlations between peak signal mass and peak STIC amplitude (Fig. 3 B), and between peak $I_{Ca(spark)}$ and peak STIC amplitude (Fig. 3 C). Two features standout in these plots. First of all, the correlation for both relationships was weak (n = 159, r = 0.056, and P = 0.487 for signal mass vs. STIC; r = −0.112 and P = 0.093 for $I_{Ca(spark)}$ vs. STIC). It is obvious that large STICs can be associated with small

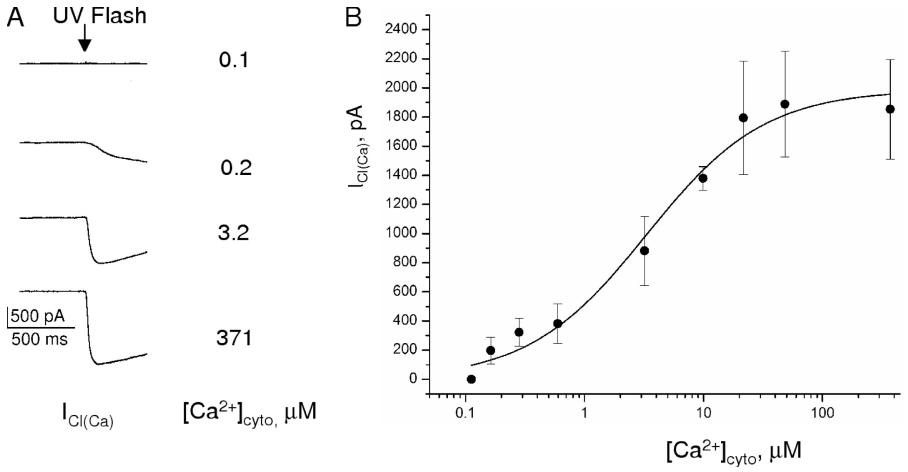

Figure 4. Characterization of $Cl_{(Ca)}$ channels using flash photolysis of NPEGTA. (A) Examples showing the response of $Cl_{(Ca)}$ channels to changes in $[Ca^{2+}]$ by flash photolysis of NPEGTA. The cells were held at −80 mV with pipette and bath solution that block K^+ currents. No fluo-3 was present in the patch pipette to eliminate possible interference of Ca^{2+} indicator to the response of $Cl_{(Ca)}$ channels to $[Ca^{2+}]$. $[Ca^{2+}]_{cyto}$ marked on the right of the traces is estimated with the parameters of endogenous fixed Ca^{2+} buffer shown in Fig. 1. (B) Dose dependence of $I_{Cl(Ca)}$ as a function of $[Ca^{2+}]$. The filled circles are averaged peak currents from the sort of experiments shown in A (N = 5–12). The solid line denotes fit to the data with Hill equation, i.e.,

$$I_{Cl(Ca)} = \frac{I_{Cl(Ca)\,max} \times [Ca^{2+}]^n}{EC_{50}{}^n + [Ca^{2+}]^n},$$

with n = 0.9 and EC_{50} = 3.3 μM.

$I_{Ca(spark)}$, and vice versa, i.e., small STICs can be activated by Ca^{2+} sparks with large $I_{Ca(spark)}$. Such independence of STIC amplitude on spark amplitude provides an indication that $Cl_{(Ca)}$ channels and RyRs may organize in such a way that the amplitude of STIC is not proportional to the area exposed to high $[Ca^{2+}]$, but is controlled by the numbers of the channels nearby the sites. This view is further strengthened by a second feature in Fig. 3 (B and C), i.e., there were 20% of Ca^{2+} sparks that did not activate STICs, i.e., STIC-less sparks. This class of sparks could be due to underlying RyRs localized deep inside of the cells so $[Ca^{2+}]$ generated is not high enough to activate $Cl_{(Ca)}$ channels on the plasma membrane. But many STIC-less sparks were observed occurring close to the plasma membrane (unpublished data). Therefore, a more plausible explanation for STIC-less sparks is that there are no $Cl_{(Ca)}$ channels present at these spark sites.

Collectively, the analyses of the relationship between Ca^{2+} sparks and STICs suggest that $Cl_{(Ca)}$ channels distribute nonuniformly on the surface membrane, and in the areas they are present, they could localize closely to RyRs where Ca^{2+} sparks occur. In the following sections, we further examine this relationship and do so in a quantitative manner.

$Cl_{(Ca)}$ Channels Are Less Sensitive to Ca^{2+} in Mouse Airway Smooth Muscle Cells than in Other Smooth Muscle Cells

The Ca^{2+} sensitivity of $Cl_{(Ca)}$ channels is one of the principal properties influencing how $Cl_{(Ca)}$ channels respond to change in $[Ca^{2+}]$ produced by Ca^{2+} sparks, thus it is a key factor needed to uncover the spatial organization of $Cl_{(Ca)}$ channels and RyRs in spark sites. Since this is the first study of $Cl_{(Ca)}$ channels in airway smooth muscle from mouse, we needed to determine this property experimentally. To do so, we studied $I_{Cl(Ca)}$ upon instantaneous and uniform elevation of $[Ca^{2+}]$ by flash photolysis of caged Ca^{2+} NPEGTA in these cells. With the experiments and the procedure described in Fig. 1 and in Materials and methods, we established the relationship between $[Ca^{2+}]_{cyto}$ and [NPEGTA] upon flash photolysis (Fig. 1 C). In our experimental conditions, when flash photolysis of NPEGTA raised $[Ca^{2+}]_{cyto}$ to <120 nM, it failed to evoke any appreciable $I_{Cl(Ca)}$ (Fig. 4 A), indicating that $Cl_{(Ca)}$ channels have a threshold >120 nM. At 0.2 μM $[Ca^{2+}]$, it started to trigger appreciable $I_{Cl(Ca)}$ with some delay; further increases in $[Ca^{2+}]$ caused $I_{Cl(Ca)}$s with greater amplitude and shorter delay of onset. At 400 μM, Ca^{2+} activated $I_{Cl(Ca)}$ instantaneously to a level of ∼2 nA. This concentration-dependent response can be better appreciated in Fig. 4 B where an averaged curve is displayed. Fitting this curve with a Hill equation yielded an apparent EC_{50} of 3.3 μM and a Hill coefficient of 0.9. To our surprise, the Ca^{2+} sensitivity of $Cl_{(Ca)}$ channels in mouse airway smooth muscle is much closer to those from *Xenopus* oocytes (EC_{50} = ∼3.5 μM at −75 mV) (Kuruma and Hartzell, 2000) and olfactory neurons (EC_{50} = ∼2.0–5 μM at around −50 mV) (Pifferi et al., 2006) than those from other types of smooth muscle (EC_{50} = 0.25–0.5 μM at −50 to −100 mV) (Pacaud et al., 1992; Wang and Kotlikoff, 1997; Piper and Large, 2003). We therefore adopted the P_o–voltage relationship of $Cl_{(Ca)}$ channels from the oocytes to derive $[Ca^{2+}]$ sensed by $Cl_{(Ca)}$ channels underlying STICs (see below).

$Cl_{(Ca)}$ Channels Underlying STICs Are Exposed to $[Ca^{2+}]$ at 2.4 μM or Greater during a Ca^{2+} Spark

Having determined the Ca^{2+} sensitivity of $Cl_{(Ca)}$ channels, it is important to estimate $[Ca^{2+}]$ "seen" by $Cl_{(Ca)}$

channels since this parameter will enable us to put spatial constraints on their distance from RyRs. We employed an approach that had successfully derived the $[Ca^{2+}]$ experienced by BK channels underlying STOCs triggered by Ca^{2+} sparks. The rationale and procedure of this approach have been described in detail previously (ZhuGe et al., 2002) and a brief description is given as following. Conductance of an STIC ($g_{(STIC)}$) is the product of $N \times P_{o(Ca,V)} \times \gamma$, where N is the number of $Cl_{(Ca)}$ channels available to a Ca^{2+} spark, γ is the unitary conductance of $Cl_{(Ca)}$ channels, and P_o is the probability of $Cl_{(Ca)}$ channel being opened and is a function of both $[Ca^{2+}]$ and voltage. Since γ is constant over a large range of voltages (Takahashi et al., 1987; Piper and Large, 2003) and N is assumed to be fixed in a given site (which is the case as shown below), $g_{(STIC)}$ becomes proportional to P_o, which in turn is a function of both $[Ca^{2+}]$ and voltage. It is demonstrated below that the amplitude of Ca^{2+} sparks is constant over a range of voltages, thus any change in $g_{(STIC)}$ at different voltages should solely reflect the voltage sensitivity of $Cl_{(Ca)}$ channels in the spark sites. Accordingly, by comparing the $g_{(STIC)}$–voltage relationship with the P_o–voltage relationship at constant $[Ca^{2+}]$ acquired in excised-patch experiments, one can deduce "apparent" $[Ca^{2+}]$ that is responsible for the activation of $Cl_{(Ca)}$ channels underlying an STIC.

(a) Voltage Dependence of $g_{(STIC)}$

Fig. 5 A displays an example, representative of nine cells, in which STICs were recorded at different voltages. At −85 mV, the leak current was −16 ± 2 pA ($n = 9$). As predicted, at the potentials more negative than −15 mV, i.e., E_{Cl}, STICs were inward; and at the potentials less negative than the E_{Cl}, they changed direction from inward to outward. (This feature is another indication that STICs result from the opening of $Cl_{(Ca)}$ channels.) For each STIC, Ohm's law can be applied to calculate its $g_{(STIC)}$, since the γ of $Cl_{(Ca)}$ channel is constant over voltages examined (Takahashi et al., 1987; Piper and Large, 2003). Fig. 5 B shows the relationship between averaged $g_{(STIC)}$ and voltage. It is worth noting that $g_{(STIC)}$ increased as voltage rose from −85 to −5 mV and then plateaued as voltage rose further (ANOVA for a general linear mixed model (Kempthorne, 1975; $P < 0.0001$). (The value for $g_{(STIC)}$ at −25 mv is omitted due to uncertainty in identifying STICs near E_{Cl}.) This pattern of change in $g_{(STIC)}$ hints that the number of $Cl_{(Ca)}$ channels for a given spark site is fixed such that the activity of these channels approaches a plateau at positive potentials. We thus scale the $g_{(STIC)}$ value at −5 mV to the maximal value of p_o activated by 40 μM Ca^{2+} from excised patches of *Xenopus* oocytes in Fig. 6.

(b) Ca^{2+} Sparks Do Not Vary at Different Voltages

The decline in $g_{(STIC)}$ at negative potentials could result from a decrease in $[Ca^{2+}]$ from Ca^{2+} sparks; we therefore measured the spark amplitude at −85 and 0 mV. The mean values of signal mass, after taking into consideration the endogenous fixed Ca^{2+} buffer, are 240,000 ± 33,000 Ca^{2+} ions at −85 mV and 258,000 ± 30,000 Ca^{2+} ions at 0 mV ($P > 0.706$; $n = 74$ at −85 mV and $n = 61$ at 0 mV). The values for $I_{Ca(spark)}$ are 4.0 ± 0.6 pA at −85 mV and 4.3 ± 0.5 pA at 0 mV ($P > 0.694$; the same n as

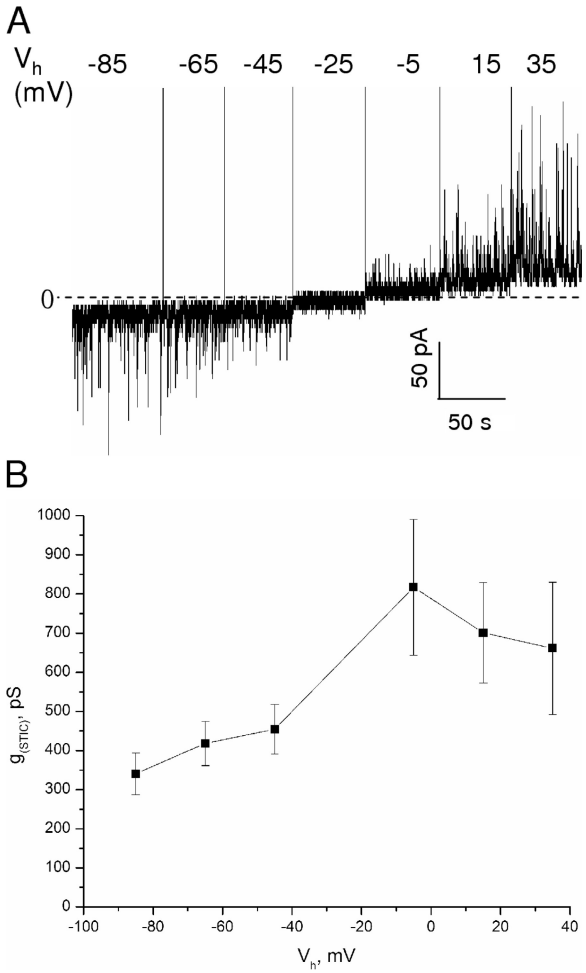

Figure 5. Voltage dependence of STIC conductance. (A) Traces of STICs recorded at different holding potentials (V_h). Note that STICs reverse from inward to outward between −25 and −5 mV, as expected for an E_{Cl} of −15 mV in this series of experiments. (B) Relationship between mean conductance of STIC ($g_{(STIC)}$) and V_h. The data were averaged across experiments ($n = 9$). The value at −25 mV in this panel was not included because the amplitudes of STICs are too small at this voltage for the parameter to be estimated with confidence. To test the voltage dependence of $g_{(STIC)}$, the values at potentials below E_{Cl} were pooled as a low voltage group and those above E_{Cl} as a high voltage group. Using analysis of variance for a general linear mixed model (Kempthorne, 1975), it was found that $g_{(STIC)}$ in the high voltage group is significantly greater than that in the low voltage group ($P < 0.0001$). Note that models were fit using restricted maximum likelihood estimation, and compliance with the distributional assumptions of the model was evaluated both with the Kolmogorov-Smirnov goodness of fit test for normality and by inspection of frequency histograms. Analyses were performed using the Mixed Procedure in the SAS 9.1.3 statistical software package.

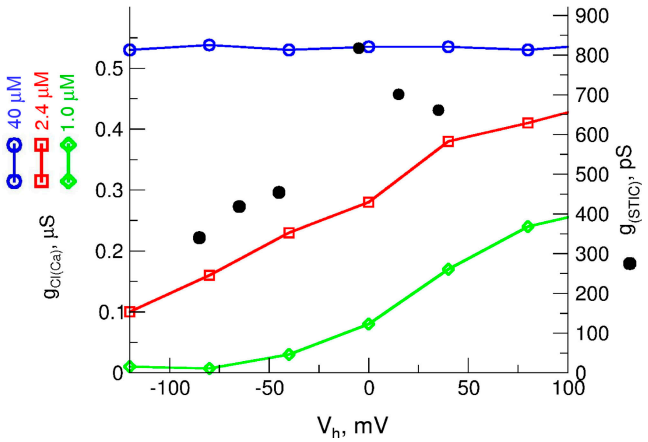

Figure 6. Comparison between voltage dependence of $g_{(STIC)}$ and P_o for $Cl_{(Ca)}$ channels. Black filled circles show $g_{(STIC)}$ (right ordinate) as a function of V_h based on the experiments in Fig. 5. The three colored lines show the relationship between the conductance of $Cl_{(Ca)}$ channels ($g_{Cl(ca)}$, left ordinate) and voltage at a constant $[Ca^{2+}]$ of 1 μM (green diamond), 2.4 μM (red square), and 40 μM (blue circle) in excised inside–outside patches of *Xenopus* oocytes (adapted from Fig. 6 B, Kuruma and Hartzell, 2000). Since for a given patch, the unitary conductance of $Cl_{(Ca)}$ channels and their number should be constant across holding potentials, the curves should reflect the relationship between P_o and voltage. Furthermore, since $g_{(STIC)}$ reaches the peak at −5 mV and $g_{Cl(Ca)}$ lacks voltage dependence at 40 μM Ca^{2+}, we scale the $g_{(STIC)}$ value at −5 mV to the $g_{Cl(Ca)}$ at 40 μM Ca^{2+}. It is worth noting that the relationship between $g_{(STIC)}$ and membrane potential follows closest to the relationship between P_o and voltage at 2.4 μM $[Ca^{2+}]$ or greater.

for signal mass). These results argue that Ca^{2+} sparks do not change their characteristics at voltages examined.

(c) Comparison of $g_{(STIC)}$–Voltage Curve and $P_{o(Cl(Ca))}$–Voltage Curves at Different $[Ca^{2+}]$

The invariance in the amplitude of Ca^{2+} sparks at different potentials suggests that the decline in $g_{(STIC)}$ could not be due to a decrease in $[Ca^{2+}]$ at negative potentials. Moreover, given that (a) the number of available $Cl_{(Ca)}$ channels appears to be fixed for a given spark site (Fig. 5 B), and that (b) γ is constant over a large range of voltages (Takahashi et al., 1987; Piper and Large, 2003), the observed $g_{(STIC)}$–voltage relationship reflects a relationship between P_o and voltage at a $[Ca^{2+}]$ produced by Ca^{2+} sparks.

To determine this $[Ca^{2+}]$, we overlaid the $g_{(STIC)}$–voltage curve with P_o–voltage curves of $Cl_{(Ca)}$ channels at known $[Ca^{2+}]$ obtained in excised patch from *Xenopus* oocytes. The P_o–voltage curves from *Xenopus* oocytes (Kuruma and Hartzell, 2000) were chosen because of the remarkable similarities in apparent EC_{50} of $Cl_{(Ca)}$ channels to Ca^{2+} between the oocytes (~3.5 μM at −75 mV) and mouse airway smooth muscle (3.3 μM at −80 mV). Also $Cl_{(Ca)}$ channels from smooth muscle exhibit a voltage dependence trend similar to those in *Xenopus* oocytes (Angermann et al., 2006). As shown in Fig. 6, the $g_{(STIC)}$–voltage curve fell closely to the P_o–voltage curve

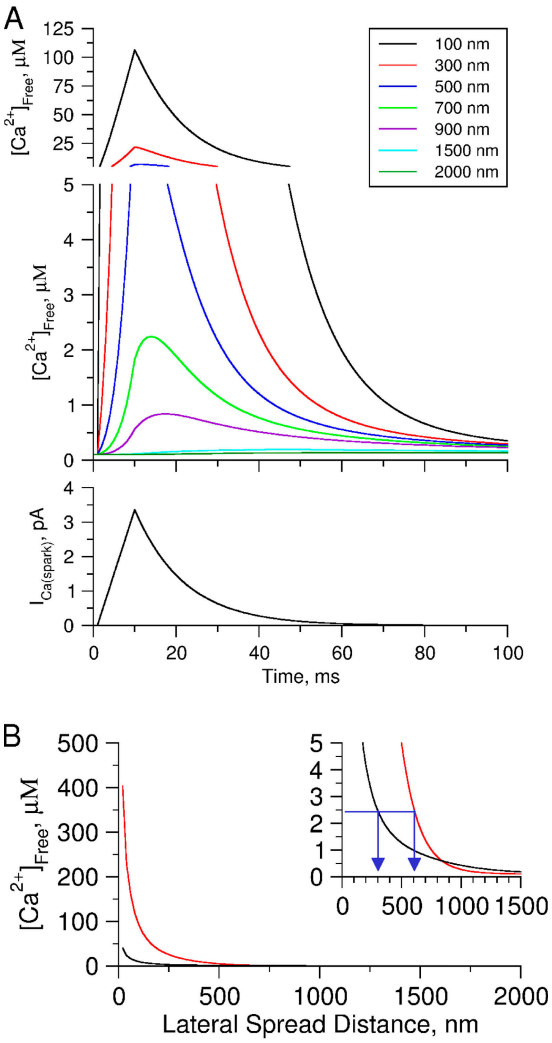

Figure 7. Area of $Cl_{(Ca)}$ channels activated by Ca^{2+} sparks as revealed by spatial and temporal profile of $[Ca^{2+}]$ derived from a simulation using measured $I_{Ca(spark)}$. (A) Spatio-temporal profile of $[Ca^{2+}]$ produced by $I_{Ca(spark)}$. Traces denote time courses of $[Ca^{2+}]$ at various distances from the release source with measured $I_{Ca(spark)}$ shown in the bottom panel. The amplitude of $I_{Ca(spark)}$, i.e., 1.2 pA as measured from averaging across the whole population of Ca^{2+} sparks in the present study, was adjusted (up to 3.5 pA) to compensate for the estimated endogenous fixed Ca^{2+} buffer with an on-rate of 8×10^4 $mM^{-1}s^{-1}$. Note that to visualize better the low end of $[Ca^{2+}]$, values >5 μM are shown at a compressed scale. (B) Spatial profile of $[Ca^{2+}]$ at the peak (red solid line) and at 40 ms (black solid line) of $I_{Ca(spark)}$. Inset is the same plot on an expanded scale in order to reveal the low end of $[Ca^{2+}]$. Blue lines with arrows mark the lateral distance from Ca^{2+} release site where $[Ca^{2+}]$ reaches 2.4 μM at two time points. Note that a several hundred fold $[Ca^{2+}]$ gradient exists within ~300 nm of the $I_{Ca(spark)}$ site of origin. This demonstrates that F/F_0, even if determined for a single pixel, fails to reflect the complex dynamics of the $[Ca^{2+}]$ generated by a Ca^{2+} spark.

for 2.4 μM $[Ca^{2+}]$. Further visual inspection suggests that the $[Ca^{2+}]$ level underlying the $g_{(STIC)}$–voltage relationship could not be as high as 40 μM, since if this were the case, there would be no change in $g_{(STIC)}$ across different voltages. Neither could the $[Ca^{2+}]$ be as low as 1 μM,

since if so, no STIC would be detected at potentials more negative than −50 mV. Thus if $Cl_{(Ca)}$ channels underlying STICs have a similar voltage sensitivity to those channels in the oocytes, then it is reasonable to conclude that on average, $Cl_{(Ca)}$ channels underlying STICs are exposed to Ca^{2+} of 2.4 μM or greater, a concentration equal to or greater than EC_{50} for these channels.

Distance from RyRs to $Cl_{(Ca)}$ Channels is within 600 nm, as Revealed by Simulation of Spatial and Temporal Profile of $[Ca^{2+}]$ Based on Measured $I_{Ca(spark)}$

With the knowledge of $[Ca^{2+}]$ "seen" by $Cl_{(Ca)}$ channels underlying STICs and the waveform and amplitude of $I_{Ca(spark)}$, we can estimate the spatial arrangement of $Cl_{(Ca)}$ channels and RyRs in Ca^{2+} spark sites. To do so, we first derived the spatio-temporal profile of $[Ca^{2+}]$ produced by Ca^{2+} sparks using measured $I_{Ca(spark)}$ as Ca^{2+} input in reaction-diffusion simulations. The parameters for simulations are provided in the Materials and methods. In brief, located at 20 nm from the plasma membrane, the spark was modeled as an ∼20 nm^3 "point" source of $I_{Ca(spark)}$s. The amplitude of $I_{Ca(spark)}$ was adjusted to compensate for the endogenous fixed Ca^{2+} buffer so that resultant [CaFluo3] equaled that measured experimentally (Fig. S1 for detail). Fig. 7 A shows the spatial and temporal profile of $[Ca^{2+}]$ produced by Ca^{2+} sparks under the estimated buffer condition. A notable feature in this profile is that, at a distance >600 nm, the $[Ca^{2+}]$ reaches its peak later and decays slower than the underlying $I_{Ca(spark)}$. At distances of <600 nm from the source, the temporal profile of $[Ca^{2+}]$ closely follows $I_{Ca(spark)}$, i.e., it rises to peak linearly and decays to the zero level exponentially.

To estimate the area that is likely occupied by $Cl_{(Ca)}$ channels near the spark sites, we plotted and examined $[Ca^{2+}]$ profiles along the plasma membrane (Fig. 7 B). Since the $[Ca^{2+}]$ profile evolves as the $I_{Ca(spark)}$ progresses, we examined the profiles at two time points, i.e., 9 ms at the peak of $I_{Ca(spark)}$ and 40 ms, which is ∼86% of STIC peak (see Fig. 2 and Table I). The profile at 9 ms shows a maximal size of Ca^{2+} domain. But at this time point $Cl_{(Ca)}$ channels might not yet be in equilibrium with Ca^{2+}. The profile at 40 ms is the result of $I_{Ca(spark)}$ when it decays near the basal level, displaying a much smaller domain size. At this point, however, $Cl_{(Ca)}$ channels should be in equilibrium with Ca^{2+} since STICs reach ∼86% of their maximal value (Fig. 2 and Table I). Thus examining Ca^{2+} profiles from these two time points should define a lower and higher boundary for the area occupied by activated $Cl_{(Ca)}$ channels in the spark sites. As shown in Fig. 7 B (red lines), at 9 ms of $I_{Ca(spark)}$, the lateral distance where $[Ca^{2+}]$ drops below 2.4 μM is ∼600 nm from the Ca^{2+} source. At 40 ms of $I_{Ca(spark)}$, this distance shrinks to 300 nm (Fig. 7 B, black lines). Therefore the area occupied by $Cl_{(Ca)}$ channels could lie in the range between 300 and 600 nm in radius.

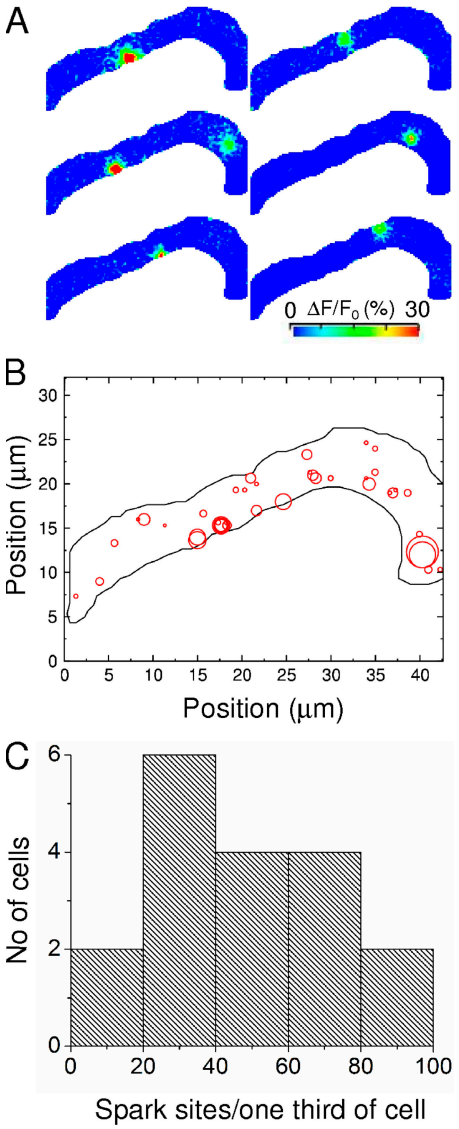

Figure 8. Number of spark-generating sites in airway smooth muscle cells. (A) Images shown are examples of Ca^{2+} sparks at their peak from a single mouse airway smooth muscle cell loaded with fluo-3 AM (5 μM) for 30 min at room temperature. Ca^{2+} fluorescence images were acquired at a rate of 67 Hz with an exposure of 5 ms per image. (B) A map of Ca^{2+} spark location and amplitude for the cell shown in A. Ca^{2+} sparks were recorded during ten 3-s periods for a total of 30 s. Each circle denotes the occurrence of one Ca^{2+} spark, and the area of the circle is proportional to the peak intensity ($\Delta F/F_0$ (%)) of the spark (not the spatial extent of the spark). (C) Histogram of number of spark-generating sites in the field of view per cell. The mean number of spark-generating sites per field of view is 36. Since approximately one third of the cell was in the field, the mean number of spark-generating sites for the entire cell is around 108.

$Cl_{(Ca)}$ Channels Concentrate Near Ca^{2+} Spark Sites at a Density of 300 Channels/μm^2

Do the areas estimated above reflect a physical domain or a functional domain for $Cl_{(Ca)}$ channels in spark sites? In other words, $Cl_{(Ca)}$ channels could be physically confined to the areas near spark sites as estimated, e.g.,

within 600 nm, or they could be uniformly distributed in the plasma membrane such that an STIC results from the activation of the channels in an area where a $[Ca^{2+}]$ reaches 2.4 μM and greater. To distinguish between these two possibilities, we compared the number of $Cl_{(Ca)}$ channels from all Ca^{2+} sparks sites and the number of $Cl_{(Ca)}$ channels in an entire cell.

To obtain the number of $Cl_{(Ca)}$ channels that can be activated by Ca^{2+} sparks from all the sites in a cell, we performed two sets of experiments. First, we determined the number of Ca^{2+} sparks sites in these cells. In line with our previous study (ZhuGe et al., 2004), we defined a spark site as an area of 333 × 333 nm; i.e., if the epicenter pixel of two sparks did not localize in the same pixel, they would be assigned to two different spark sites. Fig. 8 A displays the images when several of Ca^{2+} sparks reached their peak during a series of recordings. Notably, Ca^{2+} sparks occurred in all parts of the cell. By repeatedly acquiring images at the same speed for ten 3-s sequences, we localized each Ca^{2+} spark to construct a two-dimensional Ca^{2+} spark site map. (Imaging for longer time was avoided so as to minimize the possible bleaching by the laser of fluo-3 fluorescence.) Fig. 8 B is such a map from the cell shown in Fig. 8 A; each circle indicates the occurrence of a single spark with the center of the circle lying at the spark's epicenter pixel and the area of the circle proportional to the magnitude of $\Delta F/F_0$ at that pixel. Visual inspection of such maps makes it evident that there are many spark sites per cell. On average, the spark sites per field of observation were 36 ± 4 (N = 18, Fig. 8 C). Since roughly one third of the cell was in the field of observation, the number of sites would appear to be close to 100 per cell.

Next, we calculated the averaged number of $Cl_{(Ca)}$ channels per spark site. As indicated in Fig. 5 B, on average $g_{(STIC)}$ at −85 mV was 340 pS. This conductance could result from the opening of ∼50% of $Cl_{(Ca)}$ channels in the spark site since at positive potentials $g_{(STIC)}$ increased about onefold. This leads to an estimate that there could be as many as 340 $Cl_{(Ca)}$ channels per spark site given that each of these channels has a γ of 2 pS (Takahashi et al., 1987; Piper and Large, 2003). For a single cell with ∼80 spark sites triggering STICs (after considering 20% are STIC-less sparks), the total number of $Cl_{(Ca)}$ channels at these sites was estimated to be a minimum of 27,200.

As a second estimation of the total number of $Cl_{(Ca)}$ channels in these cells, we measured maximal $I_{Cl(Ca)}$ by raising $[Ca^{2+}]$ to 50–400 μM with flash photolysis of NPEGTA of the whole cell (see Materials and methods). We found that at −80 mV, 50 μM $[Ca^{2+}]$ activated an $I_{Cl(Ca)}$ of 1,889 ± 362 pA (N = 4) and 400 μM caused a current of 1,853 ± 342 pA (N = 7). Therefore, almost one order of magnitude of difference in $[Ca^{2+}]$ triggered $I_{Cl(ca)}$ with a similar amplitude, indicating that these levels of $[Ca^{2+}]$ most likely activate all the $Cl_{(Ca)}$ channels in the cells. If we assume $Cl_{(Ca)}$ channels have a maximum P_0 at 0.8 and a γ of 2 pS, then the total number of $Cl_{(Ca)}$ channels in a cell is ∼17,800. This estimate is in rough agreement with the first one above.

Taken together, these estimates indicate that all the $Cl_{(Ca)}$ channels in a cell could localize in the spark sites. Since the area covered by a Ca^{2+} spark where $[Ca^{2+}]$ is >2.4 μM is ∼1.13 μm^2 (a circle with 600 nm in radius) and the surface area of a cell is ∼2,800 μm^2 (given a 3-μm radius and a 150-μm length), $Cl_{(Ca)}$ channels could be present in ∼3% of plasma membrane and, moreover, in these areas the density of the channels could be as high as 300 channels/μm^2.

DISCUSSION

Since the discovery of Ca^{2+} sparks in smooth muscle more than a decade ago, researchers have focused on the pathophysiology of Ca^{2+} sparks and STOCs (Nelson et al., 1995; ZhuGe et al., 1998; Brenner et al., 2000; Amberg and Santana, 2003), but paid little attention to the functional coupling of Ca^{2+} sparks and STICs. In the current study, we have gained insight into the mechanisms generating STICs by Ca^{2+} sparks. We found that Ca^{2+} sparks trigger STICs by activating nearby $Cl_{(Ca)}$ channels that form clusters at high density in the plasma membrane. The finding represents a major step forward in understanding of how Ca^{2+} sparks activate STICs in smooth muscle.

RyRs and $Cl_{(Ca)}$ Channels Constitute a Signaling Microdomain Underlying the Activation of STICs by Ca^{2+} Sparks

Several lines of evidence suggest that $Cl_{(Ca)}$ channels highly concentrate in the surface membrane and closely couple with RyRs in Ca^{2+} spark sites. First, by analyzing and comparing the voltage dependence of STIC and $Cl_{(Ca)}$ channels, we found that during a Ca^{2+} spark, $Cl_{(Ca)}$ channels underlying STICs are exposed to a $[Ca^{2+}]$ at 2.4 μM or greater. Given the $[Ca^{2+}]$ spatial-temporal profile produced by Ca^{2+} sparks, for $Cl_{(Ca)}$ channels to be exposed to that level of $[Ca^{2+}]$, they must localize closer than a micron from RyRs, occupying an area of ∼1 μm^2. We also observed that the conductance of STIC ($g_{(STIC)}$) increases as voltage becomes less negative, but it reaches a plateau at potentials greater than −5 mV. This result indicates that the number of $Cl_{(Ca)}$ channels activated by Ca^{2+} sparks is limited, and the area occupied by these channels is confined in Ca^{2+} sparks sites. If $Cl_{(Ca)}$ channels homogenously are distributed in the surface membrane, $g_{(STIC)}$ should continue to increase as a function of voltage since these channels, though not gated by voltage, are voltage dependent (Kuruma and Hartzell, 2000; Angermann et al., 2006). Their nonhomogenous distribution is further supported by the observation that some Ca^{2+} sparks, despite their near

membrane location, fail to trigger STICs. We further demonstrated that the number of Cl^- channels present in Ca^{2+} spark sites is close to the number of all $Cl_{(Ca)}$ channels present in the entire cell. Consistent with $[Ca^{2+}]$ dropping with distance from the spark source due to diffusion and buffering, the total surface area that can be exposed to $[Ca^{2+}]$ sufficient to generate STICs is estimated to be <5% of the surface area of a cell. This strongly indicates that $Cl_{(Ca)}$ channels concentrate within 600 nm of Ca^{2+} spark sites. We estimate that the density of these channels near the spark sites can be as high as 300 channels/μm^2 given that they have a small unitary conductance of 2 pS (Takahashi et al., 1987; Piper and Large, 2003). Finally, we found that at −85 mV, STICs with amplitude >20 pA can be routinely recorded in these cells when E_{Cl} is set at −15 mV. This magnitude of STICs should result from the activation of $Cl_{(Ca)}$ channels exposed to a high $[Ca^{2+}]$, since at this potential their apparent EC_{50} to Ca^{2+} is on the order of 3 μM (Fig. 4, see below). To experience this level of $[Ca^{2+}]$, $Cl_{(Ca)}$ channels have to reside near RyRs that produce Ca^{2+} sparks, as $[Ca^{2+}]$ would drop steeply moving away from RyRs (Fig. 7).

Our notion that RyRs and $Cl_{(Ca)}$ channels form a microdomain is in line with an emerging idea that Ca^{2+}-sensitive channels cluster near to their triggers, resulting in efficient molecular coupling. For instance, BK channels appear to form clusters near RyRs in gastric smooth muscle cells (ZhuGe et al., 2002); they also cluster in the proximity of voltage-gated Ca^{2+} channels in the central nervous system (Berkefeld et al., 2006). Moreover, the clustering of these channels could undergo dynamic changes under different physiological stages. For example, in mice as pregnancy approaches term, BK channels in myometrial cells go through a transition from a clustered to a diffused distribution in the plasma membrane (Eghbali et al., 2003). This sort of transition could serve as a mechanism to fine tune the function of the channels in the cells. It will be important to determine molecular mechanisms leading to cluster formation and transition.

$Cl_{(Ca)}$ Channels Are Insensitive to Ca^{2+} in Mouse Airway Smooth Muscle

$Cl_{(Ca)}$ channels in smooth muscle are thought to be quite sensitive to Ca^{2+}, with a K_d of 0.2–0.5 μM and a threshold as low as 50 nM at negative potentials between −50 and −100 mV (Pacaud et al., 1992; Wang and Kotlikoff, 1997; Piper and Large, 2003). However, the results in the present study indicate that in mouse airway smooth muscle cells they are quite insensitive to Ca^{2+}, with an apparent EC_{50} as high as 3.3 μM at −80 mV. There are several possible reasons underlying this discrepancy. One possibility could stem from a difference in the molecular identity of $Cl_{(Ca)}$ channels among smooth muscle. It has been demonstrated that, in addition to Ca^{2+} sensitivity, $Cl_{(Ca)}$ channels in smooth muscle display variations in unitary conductance, sensitivity to kinase and phosphatase modulation, and other biophysical properties (Large and Wang, 1996; Wang and Kotlikoff, 1997; Angermann et al., 2006). These differences point to the possibility that $Cl_{(Ca)}$ channels in different smooth muscle may differ in molecular makeup. A definitive answer to this possibility awaits the identification of gene(s) for $Cl_{(Ca)}$ channels in airway smooth muscle and other smooth muscle.

Another plausible reason for the difference between our results and others' could lie in the difference in the experimental approaches used. In the present study, we employed flash photolysis of caged Ca^{2+} to raise $[Ca^{2+}]$, an approach with advantages in changing $[Ca^{2+}]$ instantaneously and uniformly. Because of these advantages, $[Ca^{2+}]$s we estimated are expected to closely reflect the concentration sensed by $Cl_{(Ca)}$ channels. However, most of the earlier studies used fura-2 to derive $[Ca^{2+}]$ over the entire cells after stimulation with agonists and voltage (e.g., Pacaud et al., 1992; Wang and Kotlikoff, 1997). Since these sorts of stimuli cause a heterogeneous increase in $[Ca^{2+}]$ (Etter et al., 1996), $[Ca^{2+}]$ "seen" by $Cl_{(Ca)}$ channels and measured by fluorescence indicators may vary significantly, leading to an overestimate of Ca^{2+} sensitivity of $Cl_{(Ca)}$ channels. It is interesting to note that when $[Ca^{2+}]_{cyto}$ was clamped to precise levels by dialyzing Ca^{2+} into cells via the patch pipette, Angermann et al. (2006) recently observed that in pulmonary smooth muscle cells, 1 μM $[Ca^{2+}]$ fails to activate $Cl_{(Ca)}$ channels at potentials more negative than E_{Cl} (0 mV), highlighting the importance of the method used to control $[Ca^{2+}]_{cyto}$ when determining the sensitivity of $Cl_{(Ca)}$ channels.

Our estimate of a low Ca^{2+} sensitivity of $Cl_{(Ca)}$ channels, based upon a fast uncaging approach, is in agreement with our measurements that these cells have a small leak current, i.e., ∼−15 pA, at −85 mV when all K^+ currents were blocked. Given a maximal total $I_{Cl(Ca)}$ of 2 nA and a resting $[Ca^{2+}]$ of ∼100 nM, this current reflects the activation of 0.5–1% $Cl_{(Ca)}$ channels, an indication that they are not very sensitive to Ca^{2+}. If they were as sensitive as previously reported, a leak current with much greater amplitude would be expected. For instance, according to one proposed $Cl_{(Ca)}$ channel kinetic model (Kuruma and Hartzell, 2000), for an apparent K_d of 250 nM, and a Hill coefficient of 3, a leak current of ∼300 pA is expected in the same recording conditions as in our experiments (unpublished data; see also Angermann et al., 2006). This value would be 20-fold greater than we measured in these cells.

Multiple RyRs Origin for Ca^{2+} Sparks Provides Insight to the Genesis and Termination of Ca^{2+} Sparks in Smooth Muscle

Many different kinds of smooth muscle produce Ca^{2+} sparks spontaneously, but there is lack of information as

to the number of RyRs underlying Ca^{2+} sparks and the mechanisms of generation and termination of Ca^{2+} sparks. In the present study, we have measured the amplitude of $I_{Ca(spark)}$ based on individual Ca^{2+} sparks recorded with high-speed imaging. With an appropriate correction for the endogenous fixed Ca^{2+} buffer, as determined in the same type of cells, we estimate that $I_{Ca(spark)}$ is 8.5 pA for a subset of Ca^{2+} sparks with the biggest amplitude and 4.1 pA for the entire population. Given a unitary current of ~0.35 pA for RyR under the quasi-physiological conditions (Mejia-Alvarez et al., 1999), the number of RyRs for Ca^{2+} sparks in smooth muscle could be on the order of 10–25. Thus, it is reasonable to conclude that Ca^{2+} sparks result from the opening of multiple RyRs in smooth muscle.

Our estimate of the waveform of $I_{Ca(spark)}$ raises a possibility that RyRs undergo a novel mechanism to generate and terminate Ca^{2+} sparks in smooth muscle. With an unprecedented temporal resolution, we uncover a unique waveform of $I_{Ca(spark)}$; that is, it reaches its peak around 9 ms and decays exponentially with a time constant of 12 ms. From our simulation, the estimated endogenous fixed Ca^{2+} buffer, although affecting the amplitude of $I_{Ca(spark)}$, does not alter the shape of this waveform in a significant way, given the assumption that this buffer has the same diffusion-limited on-rate as fluo-3. Therefore, the detected waveform likely represents the kinetic features of RyRs underlying Ca^{2+} sparks in smooth muscle. A 9-ms rising time of $I_{Ca(spark)}$ implies that the RyRs underlying Ca^{2+} sparks perhaps do not open in concert; if they do, the rise would be much faster. This result is in contrast with ideas on the genesis of Ca^{2+} sparks in skeletal and cardiac muscle, where the opening of RyRs for Ca^{2+} sparks is thought to be in concert (Cheng et al., 1996; Lacampagne et al., 1999; Zhou et al., 2005). The molecular basis for the concerted opening of RyRs in striated muscle lies in their cellular organization by forming discrete clusters in the amount of ~100 channels in the Z-disk (Block et al., 1988; Sun et al., 1995). Although not regularly arranged as in the striated muscle, RyRs in smooth muscle appear to form clusters, too, as revealed by immunolight and immunoelectron microscopy (Lesh et al., 1998; Lifshitz, L.M., J.D. Carmichael, K.D. Bellve, R.A. Tuft, K.E. Fogarty, and R. ZhuGe. 2008. *The Joint Biophysical Society 52nd Annual Meeting and 16th IUPAB International Biophysics Congress.* Abstr. 1238-Pos). Our finding of the slow activation of RyRs in clusters suggests a different gating mechanism to produce Ca^{2+} sparks in smooth muscle. (Several reports showed that Ca^{2+} sparks in smooth muscle exhibit a slower activation phase compared with those in striated muscles [Gordienko et al., 1999; Kirber et al., 2001; Ji et al., 2004; Burdyga and Wray, 2005; Liu et al., 2007; McGahon et al., 2007], but it is not known whether the rising phase of $I_{Ca(spark)}$ is also slow in those studies since no such analysis was performed.) It is interesting to note that the coupled gating of RyRs has been demonstrated in both skeletal and cardiac muscle (Marx et al., 1998, 2001), but not yet in smooth muscle. Whether lack of this type of gating is a reason for the nonconcerted opening of RyRs in smooth muscle requires further investigation.

A single exponential decay of $I_{Ca(spark)}$ indicates RyRs do not close in concert either, a finding different from that in striated muscles, where a concerted closure is also proposed (Stern and Cheng, 2004). Our observation instead suggests that Ca^{2+} sparks may be terminated as a result of stochastic closure of RyRs in the clusters. If we assume a two-state model for RyRs, we could expect that the mean open time of these channels in the clusters should be close to the decay time constant, i.e., 12 ms, of $I_{Ca(spark)}$. Remarkably, a very recent study by Laver (2007) reported that the mean open time of RyR_2 is ~10 ms when luminal $[Ca^{2+}]$ is 100 μM, a concentration that is close to $[Ca^{2+}]_{SR}$ in smooth muscle (ZhuGe et al., 1999). It is important to point out that our interpretation of termination of Ca^{2+} sparks does not rule out other possibilities, i.e., stochastic attrition of RyRs, SR Ca^{2+} depletion, RyR inactivation, and a combination of coupled gating and depletion of SR Ca^{2+}; all of them have being proposed and tested in striated muscle (Sobie et al., 2002; Stern and Cheng, 2004). However, the more complex composition of RyRs in smooth muscle, i.e., the presence of all three isoforms (Lohn et al., 2001; Yang et al., 2005) and possibly several splicing variants from each isoform, makes it likely that Ca^{2+} sparks in these cells could terminate in a way quite different from that in striated muscle.

Functional Implications of Ca^{2+} Spark Microdomains with $Cl_{(Ca)}$ Channels in Smooth Muscle

Airway smooth muscle does not generate action potential and its membrane potential usually operates in the range of −70 to −20 mV (Janssen, 2002). At these potentials, EC_{50} for $Cl_{(Ca)}$ channels should be on the order of 3 μM. For this level of Ca^{2+} sensitivity, the global $[Ca^{2+}]$ seems unable to effectively activate these channels since physiological stimulations only raise it to ~1 μM (Becker et al., 1989). Therefore it appears that $Cl_{(Ca)}$ channels, like BK channels, are not an effective target of global Ca^{2+} signaling; instead they act as the preferred target for local Ca^{2+} events. We speculate this could be a driving force that results in their localization in the vicinity of RyRs to form a microdomain. As a result, the molecular architecture of the Ca^{2+} microdomain conveys the efficiency and accuracy of $Cl_{(Ca)}$ channels in response to localized Ca^{2+} signaling. This sort of arrangement should occur in other Ca^{2+} signaling systems where local Ca^{2+} signaling is required.

We wish to thank Drs. John Walsh and Valerie DeCrescenzo for stimulating discussions and advice on the manuscript, and Dr. Stephen Baker for the statistical analyses of Fig. 5.

This study was supported by grants from the National Institutes of Health to R. ZhuGe (HL73875) and to J.V. Walsh (HL21697), and by grants from American Heart Association and Charles Hood Foundation to R. ZhuGe.

David C. Gadsby served as editor.

Submitted: 29 November 2007
Accepted: 23 May 2008

REFERENCES

Amberg, G.C., and L.F. Santana. 2003. Downregulation of the BK channel β1 subunit in genetic hypertension. *Circ. Res.* 93:965–971.

Angermann, J.E., A.R. Sanguinetti, J.L. Kenyon, N. Leblanc, and I.A. Greenwood. 2006. Mechanism of the inhibition of Ca^{2+}-activated Cl^- currents by phosphorylation in pulmonary arterial smooth muscle cells. *J. Gen. Physiol.* 128:73–87.

Becker, P.L., J.J. Singer, J.V. Walsh Jr., and F.S. Fay. 1989. Regulation of calcium concentration in voltage-clamped smooth muscle cells. *Science.* 244:211–214.

Berkefeld, H., C.A. Sailer, W. Bildl, V. Rohde, J.O. Thumfart, S. Eble, N. Klugbauer, E. Reisinger, J. Bischofberger, D. Oliver, et al. 2006. BKCa-Cav channel complexes mediate rapid and localized Ca^{2+}-activated K^+ signaling. *Science.* 314:615–620.

Block, B.A., T. Imagawa, K.P. Campbell, and C. Franzini-Armstrong. 1988. Structural evidence for direct interaction between the molecular components of the transverse tubule/sarcoplasmic reticulum junction in skeletal muscle. *J. Cell Biol.* 107:2587–2600.

Bolton, T.B., and Y. Imaizumi. 1996. Spontaneous transient outward currents in smooth muscle cells. *Cell Calcium.* 20:141–152.

Brenner, R., G.J. Perez, A.D. Bonev, D.M. Eckman, J.C. Kosek, S.W. Wiler, A.J. Patterson, M.T. Nelson, and R.W. Aldrich. 2000. Vasoregulation by the β1 subunit of the calcium-activated potassium channel. *Nature.* 407:870–876.

Burdyga, T., and S. Wray. 2005. Action potential refractory period in ureter smooth muscle is set by Ca sparks and BK channels. *Nature.* 436:559–562.

Cannell, M.B., H. Cheng, and W.J. Lederer. 1995. The control of calcium release in heart muscle. *Science.* 268:1045–1049.

Cheng, H., W.J. Lederer, and M.B. Cannell. 1993. Calcium sparks: elementary events underlying excitation-contraction coupling in heart muscle. *Science.* 262:740–744.

Cheng, H., M.R. Lederer, R.P. Xiao, A.M. Gomez, Y.Y. Zhou, B. Ziman, H. Spurgeon, E.G. Lakatta, and W.J. Lederer. 1996. Excitation-contraction coupling in heart: new insights from Ca^{2+} sparks. *Cell Calcium.* 20:129–140.

DeCrescenzo, V., R. ZhuGe, C. Velazquez-Marrero, L.M. Lifshitz, E. Custer, J. Carmichael, F.A. Lai, R.A. Tuft, K.E. Fogarty, J.R. Lemos, and J.V. Walsh Jr. 2004. Ca^{2+} syntillas, miniature Ca2+ release events in terminals of hypothalamic neurons, are increased in frequency by depolarization in the absence of Ca^{2+} influx. *J. Neurosci.* 24:1226–1235.

Eghbali, M., L. Toro, and E. Stefani. 2003. Diminished surface clustering and increased perinuclear accumulation of large conductance Ca2+-activated K+ channel in mouse myometrium with pregnancy. *J. Biol. Chem.* 278:45311–45317.

Etter, E.F., A. Minta, M. Poenie, and F.S. Fay. 1996. Near-membrane [Ca^{2+}] transients resolved using the Ca^{2+} indicator FFP18. *Proc. Natl. Acad. Sci. USA.* 93:5368–5373.

Gordienko, D.V., A.V. Zholos, and T.B. Bolton. 1999. Membrane ion channels as physiological targets for local Ca^{2+} signalling. *J. Microsc.* 196:305–316.

Harkins, A.B., N. Kurebayashi, and S.M. Baylor. 1993. Resting myoplasmic free calcium in frog skeletal muscle fibers estimated with fluo-3. *Biophys. J.* 65:865–881.

Jaggar, J.H., V.A. Porter, W.J. Lederer, and M.T. Nelson. 2000. Calcium sparks in smooth muscle. *Am. J. Physiol. Cell Physiol.* 278:C235–C256.

Janssen, L.J. 2002. Ionic mechanisms and Ca^{2+} regulation in airway smooth muscle contraction: do the data contradict dogma? *Am. J. Physiol. Lung Cell. Mol. Physiol.* 282:L1161–L1178.

Ji, G., M.E. Feldman, K.S. Greene, V. Sorrentino, H.B. Xin, and M.I. Kotlikoff. 2004. RYR2 proteins contribute to the formation of Ca^{2+} sparks in smooth muscle. *J. Gen. Physiol.* 123:377–386.

Kempthorne, O. 1975. Fixed and mixed models in the analysis of variance. *Biometrics.* 31:473–486.

Kirber, M.T., E.F. Etter, K.A. Bellve, L.M. Lifshitz, R.A. Tuft, F.S. Fay, J.V. Walsh, and K.E. Fogarty. 2001. Relationship of Ca^{2+} sparks to STOCs studied with 2D and 3D imaging in feline oesophageal smooth muscle cells. *J. Physiol.* 531:315–327.

Klein, M.G., H. Cheng, L.F. Santana, Y.H. Jiang, W.J. Lederer, and M.F. Schneider. 1996. Two mechanisms of quantized calcium release in skeletal muscle. *Nature.* 379:455–458.

Kuruma, A., and H.C. Hartzell. 2000. Bimodal control of a Ca^{2+}-activated Cl^- channel by different Ca^{2+} signals. *J. Gen. Physiol.* 115:59–80.

Lacampagne, A., C.W. Ward, M.G. Klein, and M.F. Schneider. 1999. Time course of individual Ca^{2+} sparks in frog skeletal muscle recorded at high time resolution. *J. Gen. Physiol.* 113:187–198.

Large, W.A., and Q. Wang. 1996. Characteristics and physiological role of the Ca^{2+}-activated Cl^- conductance in smooth muscle. *Am. J. Physiol.* 271:C435–C454.

Laver, D.R. 2007. Ca^{2+} stores regulate ryanodine receptor Ca^{2+} release channels via luminal and cytosolic Ca^{2+} sites. *Biophys. J.* 92:3541–3555.

Lesh, R.E., G.F. Nixon, S. Fleischer, J.A. Airey, A.P. Somlyo, and A.V. Somlyo. 1998. Localization of ryanodine receptors in smooth muscle. *Circ. Res.* 82:175–185.

Liu, Q.H., Y.M. Zheng, and Y.X. Wang. 2007. Two distinct signaling pathways for regulation of spontaneous local Ca^{2+} release by phospholipase C in airway smooth muscle cells. *Pflugers Arch.* 453:531–541.

Lohn, M., W. Jessner, M. Furstenau, M. Wellner, V. Sorrentino, H. Haller, F.C. Luft, and M. Gollasch. 2001. Regulation of calcium sparks and spontaneous transient outward currents by RyR3 in arterial vascular smooth muscle cells. *Circ. Res.* 89:1051–1057.

Lopez-Lopez, J.R., P.S. Shacklock, C.W. Balke, and W.G. Wier. 1995. Local calcium transients triggered by single L-type calcium channel currents in cardiac cells. *Science.* 268:1042–1045.

Maravall, M., Z.F. Mainen, B.L. Sabatini, and K. Svoboda. 2000. Estimating intracellular calcium concentrations and buffering without wavelength ratioing. *Biophys. J.* 78:2655–2667.

Marx, S.O., K. Ondrias, and A.R. Marks. 1998. Coupled gating between individual skeletal muscle Ca^{2+} release channels (ryanodine receptors). *Science.* 281:818–821.

Marx, S.O., J. Gaburjakova, M. Gaburjakova, C. Henrikson, K. Ondrias, and A.R. Marks. 2001. Coupled gating between cardiac calcium release channels (ryanodine receptors). *Circ. Res.* 88:1151–1158.

McGahon, M.K., D.P. Dash, A. Arora, N. Wall, J. Dawicki, D.A. Simpson, C.N. Scholfield, J.G. McGeown, and T.M. Curtis. 2007. Diabetes downregulates large-conductance Ca^{2+}-activated potassium beta 1 channel subunit in retinal arteriolar smooth muscle. *Circ. Res.* 100:703–711.

Mejia-Alvarez, R., C. Kettlun, E. Rios, M. Stern, and M. Fill. 1999. Unitary Ca^{2+} current through cardiac ryanodine receptor channels under quasi-physiological ionic conditions. *J. Gen. Physiol.* 113:177–186.

Mironneau, J., S. Arnaudeau, N. Macrez-Lepretre, and F.X. Boittin. 1996. Ca^{2+} sparks and Ca^{2+} waves activate different Ca^{2+}-dependent

ion channels in single myocytes from rat portal vein. *Cell Calcium.* 20:153–160.

Naraghi, M., and E. Neher. 1997. Linearized buffered Ca^{2+} diffusion in microdomains and its implications for calculation of $[Ca^{2+}]$ at the mouth of a calcium channel. *J. Neurosci.* 17:6961–6973.

Nelson, M.T., H. Cheng, M. Rubart, L.F. Santana, A.D. Bonev, H.J. Knot, and W.J. Lederer. 1995. Relaxation of arterial smooth muscle by calcium sparks. *Science.* 270:633–637.

Pacaud, P., G. Loirand, G. Gregoire, C. Mironneau, and J. Mironneau. 1992. Calcium-dependence of the calcium-activated chloride current in smooth muscle cells of rat portal vein. *Pflugers Arch.* 421:125–130.

Perez, G.J., A.D. Bonev, and M.T. Nelson. 2001. Micromolar Ca^{2+} from sparks activates Ca^{2+}-sensitive K^+ channels in rat cerebral artery smooth muscle. *Am. J. Physiol. Cell Physiol.* 281:C1769–C1775.

Petkov, G.V., A.D. Bonev, T.J. Heppner, R. Brenner, R.W. Aldrich, and M.T. Nelson. 2001. β1-subunit of the Ca^{2+}-activated K^+ channel regulates contractile activity of mouse urinary bladder smooth muscle. *J. Physiol.* 537:443–452.

Pifferi, S., G. Pascarella, A. Boccaccio, A. Mazzatenta, S. Gustincich, A. Menini, and S. Zucchelli. 2006. Bestrophin-2 is a candidate calcium-activated chloride channel involved in olfactory transduction. *Proc. Natl. Acad. Sci. USA.* 103:12929–12934.

Piper, A.S., and W.A. Large. 2003. Multiple conductance states of single Ca^{2+}-activated Cl^- channels in rabbit pulmonary artery smooth muscle cells. *J. Physiol.* 547:181–196.

Singer, J.J., and J.V. Walsh Jr. 1987. Characterization of calcium-activated potassium channels in single smooth muscle cells using the patch-clamp technique. *Pflugers Arch.* 408:98–111.

Sobie, E.A., K.W. Dilly, J. dos Santos Cruz, W.J. Lederer, and M.S. Jafri. 2002. Termination of cardiac Ca^{2+} sparks: an investigative mathematical model of calcium-induced calcium release. *Biophys. J.* 83:59–78.

Stern, M.D. 1992. Buffering of calcium in the vicinity of a channel pore. *Cell Calcium.* 13:183–192.

Stern, M.D., and H. Cheng. 2004. Putting out the fire: what terminates calcium-induced calcium release in cardiac muscle? *Cell Calcium.* 35:591–601.

Somlyo, A.V., and C. Franzini-Armstrong. 1985. New views of smooth muscle structure using freezing, deep-etching and rotary shadowing. *Experientia.* 41:841–856.

Sun, X.H., F. Protasi, M. Takahashi, H. Takeshima, D.G. Ferguson, and C. Franzini-Armstrong. 1995. Molecular architecture of membranes involved in excitation-contraction coupling of cardiac muscle. *J. Cell Biol.* 129:659–671.

Takahashi, T., E. Neher, and B. Sakmann. 1987. Rat brain serotonin receptors in *Xenopus* oocytes are coupled by intracellular calcium to endogenous channels. *Proc. Natl. Acad. Sci. USA.* 84:5063–5067.

Tanaka, Y., P. Meera, M. Song, H.-G. Knaus, and L. Toro. 1997. Molecular constitutes of maxi K_{Ca} channels in human coronary smooth muscle: predominant α + β subunit complexes. *J. Physiol.* 502:545–557.

Tsugorka, A., E. Rios, and L.A. Blatter. 1995. Imaging elementary events of calcium release in skeletal muscle cells. *Science.* 269:1723–1726.

Wang, Y.X., and M.I. Kotlikoff. 1997. Inactivation of calcium-activated chloride channels in smooth muscle by calcium/calmodulin-dependent protein kinase. *Proc. Natl. Acad. Sci. USA.* 94:14918–14923.

Williams, B.A., and S.M. Sims. 2007. Calcium sparks activate calcium-dependent Cl^- current in rat corpus cavernosum smooth muscle cells. *Am. J. Physiol. Cell. Physiol.* 293:C1239–C1251.

Yang, X.R., M.J. Lin, K.P. Yip, L.H. Jeyakumar, S. Fleischer, G.P. Leung, and J.S. Sham. 2005. Multiple ryanodine receptor subtypes and heterogeneous ryanodine receptor-gated Ca^{2+} stores in pulmonary arterial smooth muscle cells. *Am. J. Physiol. Lung Cell. Mol. Physiol.* 289:L338–L348.

ZhuGe, R., S.M. Sims, R.A. Tuft, K.E. Fogarty, and J.V. Walsh, Jr. 1998. Ca^{2+} sparks activate K^+ and Cl^- channels, resulting in spontaneous transient currents in guinea-pig tracheal myocytes. *J. Physiol.* 513(Pt 3):711–718.

ZhuGe, R., R.A. Tuft, K.E. Fogarty, K. Bellve, F.S. Fay, and J.V. Walsh Jr. 1999. The influence of sarcoplasmic reticulum Ca^{2+} concentration on Ca^{2+} sparks and spontaneous transient outward currents in single smooth muscle cells. *J. Gen. Physiol.* 113:215–228.

ZhuGe, R., K.E. Fogarty, R.A. Tuft, L.M. Lifshitz, K. Sayar, and J.V. Walsh, Jr. 2000. Dynamics of signaling between Ca^{2+} sparks and Ca^{2+}- activated K^+ channels studied with a novel image-based method for direct intracellular measurement of ryanodine receptor Ca^{2+} current. *J. Gen. Physiol.* 116:845–864.

ZhuGe, R., K.E. Fogarty, R.A. Tuft, and J.V. Walsh, Jr. 2002. Spontaneous transient outward currents arise from microdomains where BK channels are exposed to a mean Ca^{2+} concentration on the order of 10 μM during a Ca^{2+} spark. *J. Gen. Physiol.* 120:15–27.

ZhuGe, R., K.E. Fogarty, S.P. Baker, J.G. McCarron, R.A. Tuft, L.M. Lifshitz, and J.V. Walsh, Jr. 2004. Ca^{2+} spark sites in smooth muscle cells are numerous and differ in number of ryanodine receptors, large-conductance K^+ channels, and coupling ratio between them. *Am. J. Physiol. Cell Physiol.* 287:C1577–C1588.

ZhuGe, R., V. DeCrescenzo, V. Sorrentino, F.A. Lai, R.A. Tuft, L.M. Lifshitz, J.R. Lemos, C. Smith, K.E. Fogarty, and J.V. Walsh, Jr. 2006. Syntillas release Ca^{2+} at a site different from the microdomain where exocytosis occurs in mouse chromaffin cells. *Biophys. J.* 90:2027–2037.

Zhou, J., G. Brum, A. Gonzalez, B.S. Launikonis, M.D. Stern, and E. Rios. 2005. Concerted vs. sequential. Two activation patterns of vast arrays of intracellular Ca^{2+} channels in muscle. *J. Gen. Physiol.* 126:301–309.

Zhou, Z., and E. Neher. 1993. Mobile and immobile calcium buffers in bovine adrenal chromaffin cells. *J. Physiol.* 469:245–273.